Monthly Notices of the ROYAL ASTRONOMICAL SOCIETY

MNRAS **529,** 3121–3139 (2024) https://doi.org/10.1093/mnras/stae238
Advance Access publication 2024 January 22

Cassini's CDA observes a variety of dust populations just outside Saturn's main rings

Simon Linti,[1★†] Nozair Khawaja,[1★†] Jon K. Hillier,[1] Lenz Nölle,[1] Christian Fischer,[2] Hsiang-Wen Hsu,[3] Ralf Srama[4] and Frank Postberg[1]

[1]*Institut für Geologische Wissenschaften, Freie Universität Berlin, Malteserstraße 74-100, D-12249 Berlin, Germany*
[2]*Institut für Geowissenschaften, Ruprecht-Karls-Universität Heidelberg, Im Neuenheimer Feld 234-236, D-69120 Heidelberg, Germany*
[3]*Laboratory for Atmospheric and Space Physics, University of Colorado, 1234 Innovation Dr, Boulder, CO 80303, USA*
[4]*Institut für Raumfahrtsysteme, Universität Stuttgart, Pfaffenwaldring 29, D-70569 Stuttgart, Germany*

Accepted 2024 January 19. Received 2024 January 17; in original form 2023 July 31

ABSTRACT

Before the end of its mission, the Cassini spacecraft orbited Saturn in a series of highly inclined elliptical 'Ring-Grazing' orbits (RGO). During the RGO, the spacecraft passed repeatedly through the ring plane outside the F ring, near the orbits of Janus and Epimetheus, at an average relative speed of ∼20 km s^{-1}. For the first time, Cassini's Cosmic Dust Analyser (CDA) directly sampled dust particles from this region. Here, we analyse the compositions of dust grains sampled within ±15 min relative to nine ring plane crossings of the RGO. The compositions of most analysed RGO grains are similar to those of E ring ice grains, implying that the E ring extends to within at least 2.45 Saturn radii (R_S) of Saturn. The compositional distribution of these grains point at a similar average period (decades) since ejection from Enceladus as of particles in the outer E ring (beyond 8 R_S). Higher fractions of larger grains are found near the orbits of Janus and Epimetheus, which probably represent ejecta from these moons. Most of these grains have compositions similar to the background E ring grains, indicating that E ring material is coating the surfaces of Janus and Epimetheus. We also report the detection of several types of mineral grains on prograde orbits, one of which, a water ice/silicate mixture, has never been observed by CDA elsewhere. These mineral grains appear to have a different origin from the E ring, and may arise from nearby moons, the F ring, or main rings.

Key words: methods: data analysis – planets and satellites: individual: Saturn – planets and satellites: rings.

1 INTRODUCTION

Launched in 1997, the Cassini–Huygens space mission explored Saturn, its rings, and moons. A suite of 12 instruments on the spacecraft included mass spectrometers for the compositional analysis of dust and gas (Srama et al. 2004; Waite et al. 2004). Over a period of 13 yr, the Cosmic Dust Analyser (CDA; Srama et al. 2004) sampled ice grains in Saturn's E ring (Hillier et al. 2007; Postberg et al. 2008; Grün, Krüger & Srama 2019) and from the Enceladus plume during flybys (Khawaja, Postberg & Schmidt 2017; Postberg et al. 2018; Khawaja et al. 2019). In addition, CDA detected interstellar dust (ISD) particles entering the Saturnian system from the local interstellar cloud (Altobelli et al. 2016). The analysis of thousands of E ring ice grain spectra revealed three major compositional types of ice grains: almost pure water ice, organic-enriched and salt-rich (Hillier et al. 2007; Postberg et al. 2008, 2009b, 2018; Khawaja et al. 2019).

The CDA (Srama et al. 2004), designed to sample dust in the Saturnian system, consisted of the High Rate Detector (HRD) and the Dust Analyser (DA; Fig. 1). The DA was sensitive to impacting ice and mineral (sub) micron dust grains. It consisted of three subsystems: the entrance grid (Auer et al. 2002), the Impact Ionization Detector (IID; Grün et al. 1992a,b) and the Chemical Analyser (CA), a time-of-flight (TOF) mass spectrometer (Ratcliff et al. 1992). Here, particles hitting the rhodium Chemical Analyser Target (CAT) at the bottom of the CA, at relative speeds greater than 2 km s^{-1}, were evaporated and partially ionized, generating cations which were then accelerated towards an ion detector, the multiplier. The varying arrival times of different mass, singly charged, cations at the multiplier then produced a TOF mass spectrum.

Before the end of its mission in 2017, the Cassini spacecraft explored the inner Saturnian system on two distinct sets of orbits: (i) just outside the main rings at orbital inclinations of ∼60° with respect to the ring plane (called the Ring-Grazing orbits, RGO) and (ii) between the rings and the planet at orbital inclinations of about 63° (called the Grand Finale orbits, GFO). CDA data from the latter have already been presented (Hsu et al. 2018), whereas the data from the RGO have not yet been published prior to this study. What makes these orbits interesting is that the spacecraft passed 20 times relatively close to the orbits of Janus and Epimetheus between 2016 November 30 and 2017 April 19, which provided valuable remote-sensing data (Buratti et al. 2019), and sampled the region around the dusty Janus/Epimetheus ring.

★ E-mail: s.linti@fu-berlin.de (SL); nozair.khawaja@fu-berlin.de (NK)
† These authors contributed equally.

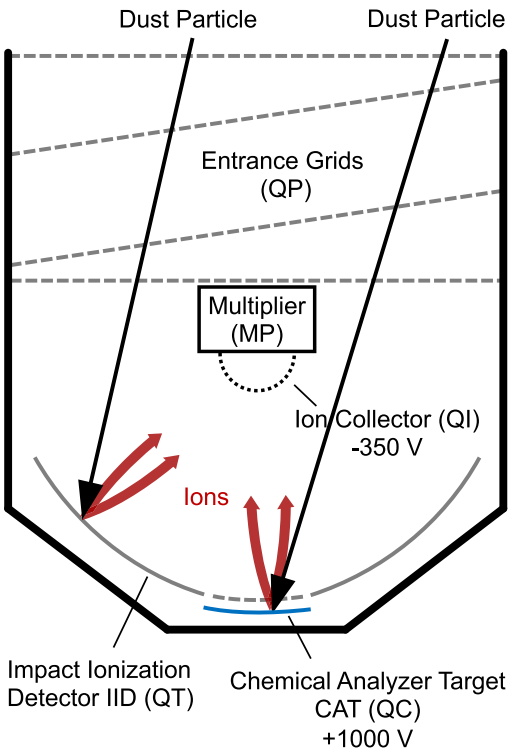

Figure 1. Cross-section of the Dust Analyser subsystem showing dust particles hitting the CAT and the IID. High-resolution spectra are only generated after impacts on to the CAT (adapted from Srama et al. 2004).

Close flybys of small moons (Pan, Daphnis, Atlas, Pandora, and Epimetheus) were performed in this phase of the mission, during which their optical properties including colour, albedo, and also visible-infrared spectral characteristics were acquired (e.g. Buratti et al. 2019). The colours of these moons vary with Saturnian distance, with those closer to Saturn redder, and more similar to the main rings. Pan is the reddest, with redness decreasing out to Pandora, and Epimetheus' colour more like those of the mid-sized moons. Buratti et al. (2019) suggested that these colour changes could be due to the ongoing accretion of icy material migrating inwards from the E ring towards the F ring and beyond. However, a detailed compositional analysis of ice and mineral dust grains sampled during these final orbits of Cassini close to the orbits of Janus and Epimetheus has until now not been conducted, and thus is the focus of this work.

The typical diameter of the F ring core is ∼10 km (Albers et al. 2012) and it is located 3400 km outside Saturn's main ring system. Two 'shepherd' moons, Prometheus and Pandora, orbit Saturn close to the F ring (Gehrels et al. 1980; Smith et al. 1981), whereas the two co-orbital moons Janus and Epimetheus, build their own faint ring outside the F ring, which was subject of previous studies (e.g. Porco 2006; Horányi et al. 2009; Williams & Murray 2011; Winter et al. 2018; Ye et al. 2018; Buratti et al. 2019), and swap positions every 4 yr (Smith et al. 1981).

So far, the exact composition of F ring material and of the nearest moons has not been investigated in situ. We report for the first time the compositional analysis of ice grains encountered during nine RGO near the orbits of Janus and Epimetheus. The outcome of this analysis could be used to investigate the origin of these grains, and in turn address questions such as: Is it possible to differentiate ejecta particles from the surfaces of Janus and Epimetheus from other particles in that region? Is there any influence from the E ring or the main rings on the composition of the sampled particles?

The technique used by CDA to analyse the compositions of encountered dust grains – namely impact ionization mass spectrometry – is relatively unusual. Therefore, before we discuss the results of the analysis, we first describe the instrument, the relevant data sets and how they were processed in Section 2. In Section 3, we then present the various encountered compositional particle types, elaborate on their spatial distributions, and analyse the elemental composition and dynamical properties of the non-icy fraction. In Section 4, we discuss the implications of these data, including the influence of the E ring and the Janus/Epimetheus ring on to the sampled region, the relative abundances of the different particle types (also in comparison to observations in the E ring), and the composition and origin of the mineral particles by comparing their properties to those of mineral particles sampled by CDA throughout the Saturnian system.

2 METHODS

This section introduces the working principle of CDA's CA subsystem and gives an overview of the observational parameters during the analysed RGO profiles (Section 2.1), followed by an explanation of the processing and compositional classification of the data (Section 2.2). We elaborate on the connection of impact ion yield and mass of the sampled particles (Section 2.3) and describe the technique used to infer the dynamical properties of the particles (Section 2.4).

2.1 Instrument settings and data acquisition/observation

The CA (Fig. 1) was a linear TOF-mass spectrometer subsystem of the CDA (Srama et al. 2004). Individual dust impacts on to the CAT (signal QC) at relative speeds above 2 km s^{-1} generated an impact plasma, the cation component of which was accelerated towards an ion detector by a 1 kV potential difference, with the anion component (including electrons) collected by the impact target itself. The CAT had a diameter of 160 mm and the short compact ion optics (flight path length ∼230 mm) resulted in a low mass resolution ($m/\Delta m$) of 20–50. The impact charge of individual impacts was amplified by charge sensitive amplifiers (or electron multiplier in the case of the QM channel) and all three signals QC, QI, and QM were recorded over time. Spectrum recording was initiated by signals exceeding individual thresholds in one or more of the three channels, by either a large charge signal at the target (QC; electrons and negative ions), a large ion signal at the ion grid (QI) in front of the multiplier, or charge above a certain threshold arriving at the multiplier (QM). The QT signal is attributed to the target of the IID, another subsystem of the DA. Similar to the CAT, it measured the charge of impacting particles, however, no spectra with compositional information are produced in such cases and the signal is thus irrelevant for this work.

The trigger mechanism was defined by the flight software, which determined which channels were monitoring for event recording. As the charge generated by an impact is a function of the impacting grain's mass and impact speed, adjustments to the charge thresholds used for triggering led to changes in the sensitivity of the DA to different grain mass and velocity regimes. Table 1shows the trigger settings used during the various ring plane crossings. With high impact rates expected, the event trigger definition was set to the impact targets (QC_QT) or the multiplier (QM) only. Using only the multiplier signal as a trigger condition is a robust procedure for avoiding false triggering on plasma-induced disturbances at the instrument electrodes.

Table 1. List of orbits used for this work. The parameters are the RPX date and time, the distances to multiple reference points (Saturn, and average semimajor axes of both the F ring and the Janus/Epimetheus orbits), the angle between the boresight of the instrument and dust on circular prograde orbits (ram angle, Khalisi, Srama & Grün 2015), the instrument trigger setting (QC_QT: both impact targets were used for event triggering, QM: only the multiplier signal was used for triggering), and whether the QI focusing field in front of the multiplier was switched on. 1 R_S (Saturn radius) = 60 268 km.

UTC (RPX)	RPX distance to Saturn (R_S)	RPX distance to F ring (km)	RPX distance to Janus/Epimetheus orbits (km)	Ram angle (°)	Trigger setting	QI focusing field (V)
2016–361T01:31:12	2.489	9804	1426	9.74	QC_QT	–350
2017–009T09:20:21	2.484	9464	1766	13.17	QC_QT	–350
2017–016T13:12:06	2.485	9524	1706	19.20	QC_QT	–350
2017–023T17:05:25	2.485	9537	1693	1.61	QC_QT	–350
2017–045T05:56:42	2.506	10 798	432	14.70	QM	–350
2017–081T01:57:16	2.457	7870	3360	5.42	QM	0
2017–088T05:48:41	2.456	7789	3441	17.47	QM	–350
2017–095T09:40:03	2.457	7878	3352	3.70	QM	–350
2017–109T17:44:25	2.462	8179	3051	0.81	QM	0

Table 2. Relative abundances of the spectral types including unused spectra.

Spectral type	Type 1	Type 2	Type 3	Type 4	Type 5	Weak	Unidentifiable
Spectra	1644	237	51	27	41	21	86
Fraction (per cent)	78.0	11.2	2.4	1.3	1.9	1.0	4.1

For this analysis, the TOF mass spectra of nine RGO (Table 1) recorded within ±15 min with respect to the ring plane crossing (RPX) time were used. During these passages of the ring plane, the relative impact speed was always close to the spacecraft speed of ∼20 km s^{-1}. As mentioned above, the CDA settings for triggering the spectrum recording had an influence on the detection of particle size regimes. The QC_QT trigger between DOY 2016–361 and DOY 2017–023 resulted in the preferential detection of bigger particles, whereas the QM trigger applied between DOY 2017–45 and 2017–109, was more suitable for the detection of smaller particles. During the nine RPXs, the distance to the F ring varied by approximately 3000 km. During all orbits Cassini crossed the faint Janus/Epimetheus ring, coming very close to the moons' orbits during the RPX of DOY 2017–45 (Table 1). Based on the different RPX distances and the instrument settings, three orbit groups can be defined (a) DOY 2016–361, 2017–9, 16 and 23, (b) DOY 2017–81, 88, 95 and 109, and (c) DOY 2017–45.

2.2 Spectral calibration and selection criteria

In total 2107 spectra were initially considered in this work, of which 94.9 per cent could be categorized into one of five compositional types, based on the presence of characteristic peaks corresponding to a certain composition (see below). The remaining 5.1 per cent were found to be unsuitable for further evaluation. From this unsuitable category, the 'weak' category (1 per cent) contains spectra with low signal-to-noise ratios (S/N) and hence is not included in the compositional analysis. The other 4.1 per cent are spectra deemed 'unidentifiable', because their spectra are distorted due to the high accumulated ion yield (> ∼1 pC). The majority of spectra, however, can be assigned to one of the following spectral types (Table 2), with the applied nomenclature based on spectral classification originally derived for measurements obtained in the E ring (Postberg et al. 2008, 2009b; Nölle et al. 2024), where ice particles were detected with lower impact speeds (typically 4–15 km s^{-1}). Most of the spectra recorded during the RGO possess mass lines due to Na^+ and K^+, elements that are typical contaminants from the instrument target. A mass line corresponding to Rh^+ represents the target material itself, which is ionized by particles impacting at speeds above ∼8 km s^{-1} (Postberg et al. 2009a). The high impact speeds of ∼20 km s^{-1} during the RPXs enable additional mass lines, such as C^+, O^+, and $O_2{}^+$, which in part represent target contamination (Postberg et al. 2009a), to be often observed in this data set. The mass lines O^+ and $O_2{}^+$ can also originate from water molecules, dissociated at such high impact speeds, or from silicate particle impacts. The identified compositional types are defined as

(i) Type 1: Almost pure water ice, defined by the presence of the hydronium $[H_3O]^+$ peak at 19 u. Due to the high particle impact speeds, no water clusters $[(H_2O)_{n>0}\ H_3O]^+$ are observed, unlike in most E ring spectra (Hillier et al. 2007; Postberg et al. 2008). In many cases, the water molecules fragment into O^+, OH^+ in addition to $[H_2O]^+$ and $[H_3O]^+$ sometimes causing a quadruplet of neighbouring peaks at 16–19 u. Na^+ and K^+ are generally visible in these spectra and probably represent target contamination, as stated above.

(ii) Type 2: Water ice with organics. Type 2 spectra are defined by an organic-related feature ranging from 27 to 31 u. Due to the high impact speed, only in rare cases are additional larger organic fragments, potentially aromatic, observed. Hydronium, $[H_3O]^+$ at 19 u, is always present along with an extension to lower masses representing molecular fragments. Na^+ and K^+ from target contamination are generally also visible in this type of spectra.

(iii) Type 3: Salt-rich water ice. Spectra defined by the presence of a sodium hydroxide cluster $[Na(NaOH)]^+$ at 63 u together with a large Na^+ signal, which is much larger than found in Type 1 and Type 2 spectra. A small fraction of the spectra possess an additional peak at 81 u, which is a sodium chloride cluster $[Na(NaCl)]^+$.

(iv) Type 4: Mineral spectra defined by the presence of a selection of mineral-forming ions, e.g. Mg^+, Si^+, Ca^+, and Fe^+. A fraction of these spectra exhibit an additional water feature between 16 and 19 u.

(v) Type 5: Spectra with only two mass lines from Na^+ and K^+, in addition ions from possible contaminants (H, C, O) and target material (Rh). These grains are proposed to have even higher concentrations of Na salts than Type 3 particles (Nölle et al. 2024).

2.3 Ion yield and particle size

Using an ion collector grid in front of the multiplier, CDA also measured the impact cation yield (QI). This depends on the impact speed, the composition, and the particle mass (Auer & Sitte 1968; Ratcliff et al. 1992; Srama et al. 2004).

Depending on grain composition and the impact speed, the production rate of ions can vary significantly. Analogue laboratory experiments (Wiederschein et al. 2015) indicate that, for the same particle mass and impact speed, salt-rich particles (Type 3) produce more ions on impact than pure water ice particles (Type 1). This must be considered, when calculating particle radii from instrument charge measurements. Typically, spherical particles, an approximate mean density of 1000 kg m^{-3} (Postberg et al. 2008) for all water ice dominated grains (Types 1–3 and 5), and an average bulk density of 3000 kg m^{-3} for the mineral species (Type 4) is assumed.

The relationship between particle mass and QI is given by (Srama et al. 2004)

$$m = 48.2 \times \left(\frac{\mathrm{QI}}{v^5}\right)^{0.91}, \quad (1)$$

where m is the particle mass in kg, QI is the ion yield in Coulomb, and v is the impact speed in km s^{-1} (here similar to the spacecraft speed relative to the dust ram of ∼20 km s^{-1}).

Note, that there are significant uncertainties in this mass calibration, and the particle mass is a strong function of the impact speed, so the particle sizes are only approximations. Also, since the particle mass calibration was carried out using iron particle acceleration experiments, the derived values for the mineral grains are expected to be more accurate than for the icy grains.

2.4 Modelling of particle dynamics

To determine dust particle dynamics, their orbital parameters have to be reconstructed; however, the particle trajectories prior to impact are poorly constrained. As the impact velocity is not directly measured, the range of possible impact velocities are instead inferred from spectral appearance (e.g. Postberg et al. 2009a) and expected spacecraft and particle dynamics. In this case, this results in a minimum impact speed of 19 km s^{-1} and a maximum impact speed of ∼32 km s^{-1} (the Solar system escape velocity at the detection point). Impact direction is constrained by the pointing of the instrument, its sensitive area (a function of impact angle, Srama et al. 2004) and the 28° opening angle for impacts on to the CAT. By iterating and summing over all possible velocities and angles, in combination with the available sensitive area, it is possible to derive an orbital probability distribution density map for individual particles.

3 RESULTS

In this section, we present a detailed compositional and spatial analysis of the icy and non-icy particles, encountered during the RGO. After the composition of the different water ice species (Section 3.1), we examine the properties of sampled mineral particles (Section 3.2). This also includes a model of the orbital parameters of this non-icy fraction, providing important constraints on their dynamics that are needed for a subsequent interpretation of potential particle sources. We present several properties of the particles as seen over the analysed profile (Section 3.3) and take a detailed look at the findings of the orbit, during which Cassini came closest to the orbits of Janus and Epimetheus. Finally, the chapter includes an analysis of abundances of rhodium ions from the CDA's target material ionized by impacting particles (Section 3.4), providing insights into structural properties of the impacting particles.

3.1 Water ice grains

The majority (>90 per cent) of particles detected during the RGO have compositions similar to those of ice grain types previously detected in the E ring: pure water ice (Type 1), organic-enriched ice (Type 2) and salt-rich ice (Types 3 and 5). However, the significantly higher impact speeds during the RGO influence the peak shapes and spectral appearance. In Fig. 2, we compare the features of four spectral types of E ring grains with those detected during the RGO. E ring spectra recorded with the highest impact speeds in the entire E ring data set (15–18 km s^{-1}) were chosen, similar to the impact conditions that produced the RGO spectra (impact speeds of about 20 km s^{-1}). The comparison shows that most detected particles in the vicinity of the F ring and the nearby moons have spectral features similar to those of E ring particles.

Type 1 spectra are defined by the presence of water peaks, which in this data set – with impact speeds of ∼20 km s^{-1} – are mostly $[H_3O]^+$. Other peaks observed in this, and all other spectral classes are related to contamination (Na^+, K^+, partially C^+) or target material (Rh^+), however, are not present in each spectrum. Type 2 is also water ice dominated and has similar features to Type 1, with additional organic fragments in the mass range of 27–31 u. They are related to hydrocarbon species and/or oxygen-carrying ions, such as $[CH_3O]^+$ (Khawaja et al. 2019). Type 3 spectra are water ice spectra from grains with high sodium content (Postberg et al. 2009b). In this high impact speed regime, Type 3 spectra are generally characterized by a Na^+ mass line and a sodium-sodium hydroxide cluster $[Na(NaOH)]^+$ peak at 63 u. In about 15 per cent of the spectra a cluster peak at 81 u is observed, which is from sodiated sodium chloride $[Na(NaCl)]^+$. Type 5 spectra show Na^+ and K^+ mass lines with varying amplitudes. The absence of Rh^+ in the shown Type 3 and Type 5 spectra is significant and is investigated in Section 3.4. Although also C^+ exhibits varying amplitudes in the example spectra (Fig. 2), we could not find any conclusive trend with particle type.

Both salt-bearing types (Types 3 and 5, see Section 2.2) are assumed to originate in the E ring, with only Type 3 grains having recently originated from Enceladus. Type 5 has a higher salt content (Nölle et al. 2024) and presumably are processed Type 3 particles, which evolve through water ice sputter erosion (Nölle et al. 2024) by Saturn's magnetospheric plasma (Jurac, Johnson & Richardson 2001a; Jurac et al. 2001b; Johnson et al. 2008), increasing the salt concentration from about 1 to above 10 per cent. This eventually turns their spectral appearance from Type 3 into Type 5 (Nölle et al. 2024).

3.2 Mineral grains

CDA detected 27 mineral particles (Type 4) during the RGO, which can be further divided into four subtypes based on their spectral features (Fig. 3, Tables 3 and S1). The original definition of Type 4 is based on mineral grains encountered by CDA during Cassini's orbital tour of the E ring (Nölle et al. 2024). Those grains, however, were found to be mostly on retrograde or nearly polar trajectories (Fischer et al. 2018; Trieloff et al. 2023) and therefore possess different dynamical properties than the prograde icy E ring dust. Using the techniques described in Section 2.4, we find that the mineral grains detected during the RGO are on prograde trajectories with relatively low inclinations (Fig. 4), which is a main difference to the non-prograde mineral dust encountered in the E ring (see Section 4.4).

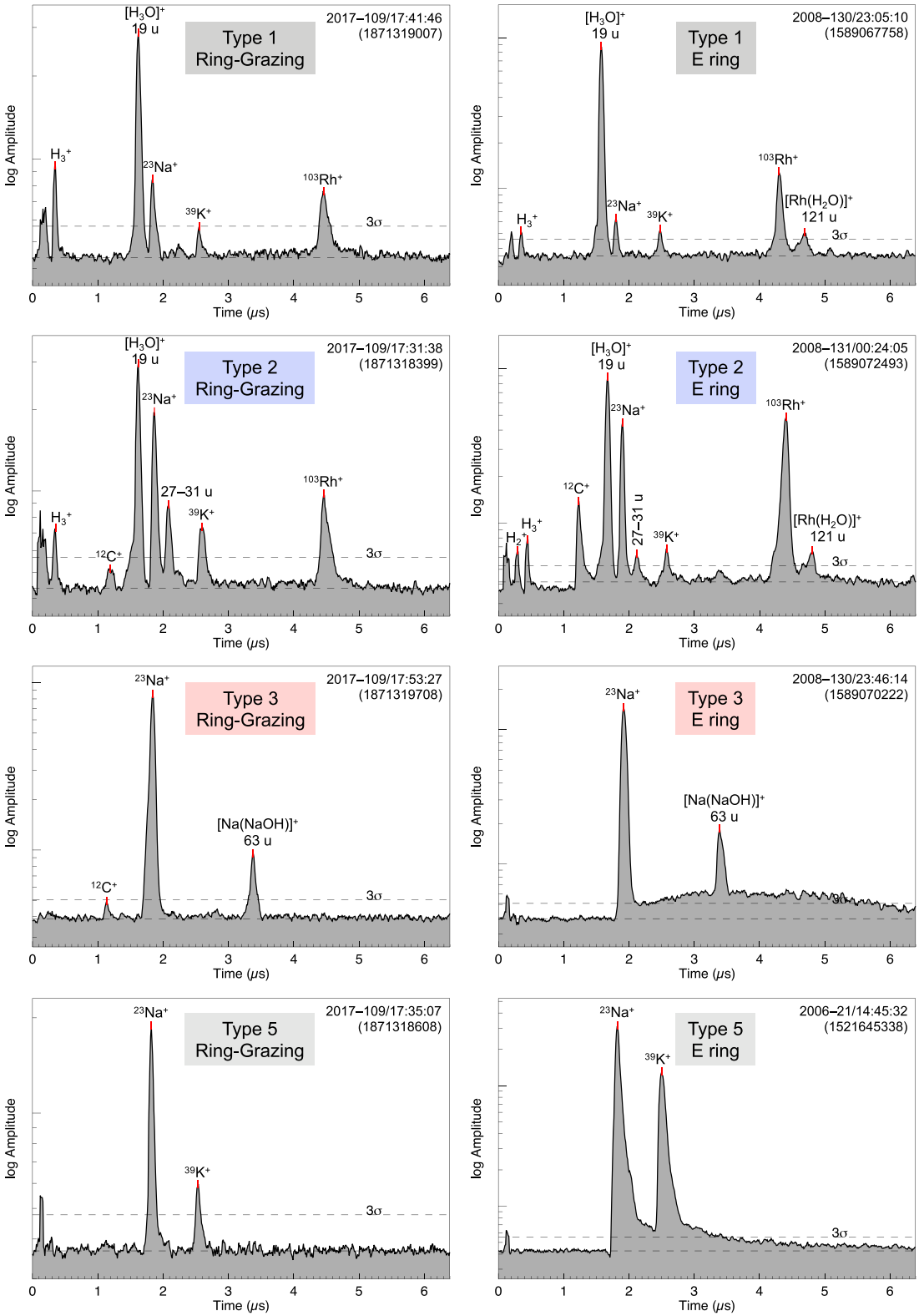

Figure 2. Comparison of the compositional Types 1–3 and 5 from the RGO (left column) with high-speed spectra recorded in the E ring (right column). The spectra show no systematic differences with radial distance to the moons. Thus, all example spectra on the left were chosen from DOY 2017–109. The upper dashed line represents the significance level of 3σ above the average spectrum noise (lower dashed line).

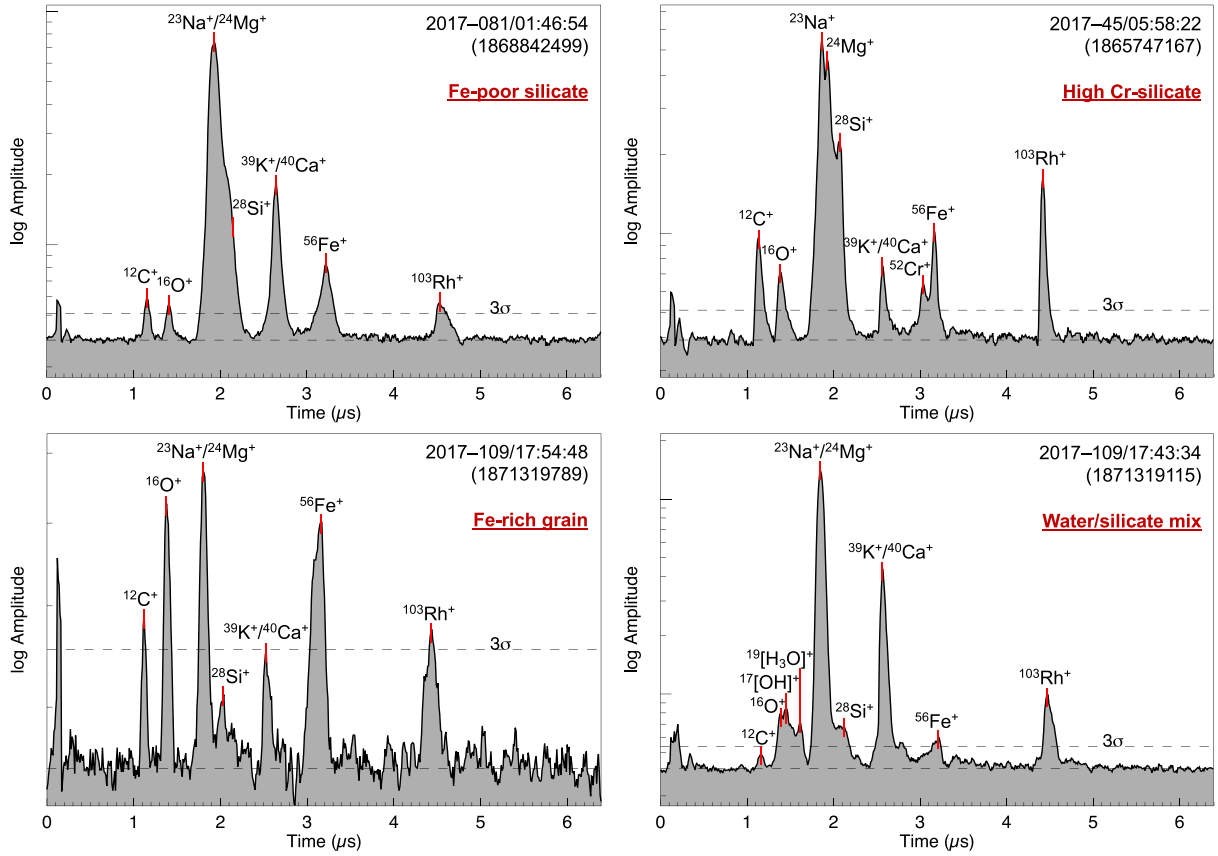

Figure 3. Example spectra for the four mineral dust subtypes detected during the RGO: Fe-poor silicate (top left), high Cr-silicate (top right), Fe-rich grain (lower left) and water/silicate mix grain (lower right). As in Fig. 2, the upper dashed line represents 3σ significance level above the average spectrum noise.

Table 3. Abundances of mineral dust particles encountered during the RGO, and element ratios (main isotopes) inferred from co-added spectra of the four subtypes. The element ratios were determined from peak amplitudes of the respective main isotopes by applying relative sensitivity factors (Fiege et al. 2014). The errors represent the difference from the determined mean value to the highest and lowest ratio determined in the individual mass spectra (Fig. S1). For comparison, the main isotope ratios of CI chondrites are given (adapted from Lodders 2003).

Type 4 subtype	Fe-poor silicate	High Cr-silicate	Fe-rich (silicate or oxide)	Water/silicate	CI chondrite
Spectra	9	4	3	11	–
Fraction (per cent)	33	15	11	41	–
$^{56}Fe/^{24}Mg$	$0.20\ ^{+0.69}_{-0.19}$	$0.26\ ^{+0.19}_{-0.20}$	–	$0.09\ ^{+0.46}_{-0.05}$	2.21 ± 0.04
$^{56}Fe/^{40}Ca$	$1.89\ ^{+13.08}_{-1.64}$	$0.91\ ^{+17.64}_{-0.76}$	$37.69\ ^{+26.90}_{-22.24}$	$0.51\ ^{+12.32}_{-0.25}$	19.08 ± 0.20
$^{56}Fe/^{28}Si$	$0.53\ ^{+1.43}_{-0.48}$	$0.15\ ^{+0.43}_{-0.13}$	$5.30\ ^{+3.79}_{-2.02}$	$0.65\ ^{+0.86}_{-0.25}$	1.71 ± 0.03
$^{24}Mg/^{28}Si$	$2.65\ ^{+5.69}_{-1.75}$	$0.58\ ^{+2.00}_{-0.18}$	–	$7.14\ ^{+4.94}_{-4.40}$	0.77 ± 0.02
$^{52}Cr/^{56}Fe$	–	$0.19\ ^{+0.12}_{-0.06}$	–	–	0.01 ± 0.001

Most mineral grains detected during the RGO (Fig. 3) are Mg-rich silicates with relatively low Fe content, when compared to e.g. CI chondritic values (Table 3). Their spectra typically show mass lines of mineral-forming ions like Mg^+, Si^+, Ca^+, and Fe^+, although not all of them must appear in every spectrum. The presence of Na^+ and K^+ in the spectra from contamination, or to a certain extent from the particles themselves, cannot be ruled out due to the low-mass resolution of CDA (Srama et al. 2004), leading to overlaps of the Na^+ and K^+ peaks with the neighbouring mass lines of Mg^+ and Ca^+, respectively. Some spectra have unique features, suggesting variations in particle composition. Four spectra, detected during three different orbits (two in DOY 2017–109, one each in DOY 2017–45 and 2017–23), show an additional mass line at 52 u, which might be due to Cr^+ ions (Fig. 3, top right). Another 11 Mg-rich spectra (Fig. 3, lower right) contain a distinct water feature peak from 16 to 19 u, which has never previously been observed together with mineral features elsewhere in the Saturnian system (Fischer et al. 2018; Trieloff et al. 2023). This indicates either the existence of hydrous mineral species, or water/silicate mixed phases in the vicinity of the F ring and the nearby moons, as seven of these spectra

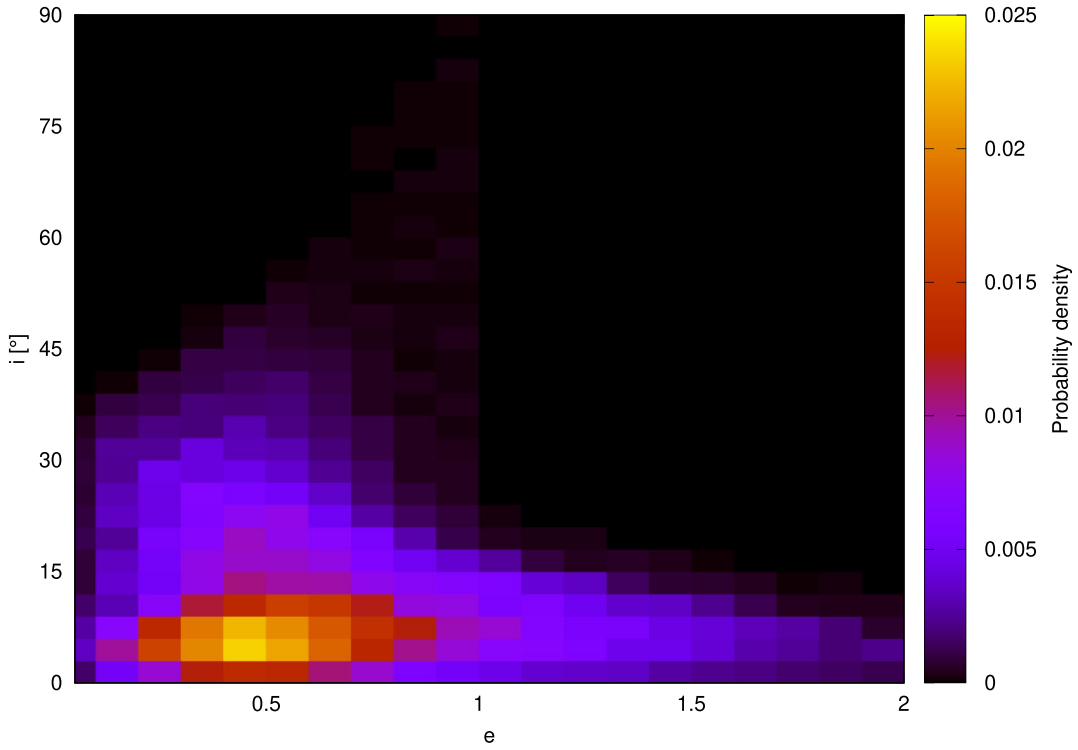

Figure 4. Modelled eccentricity e and inclination i (°) probability density distribution (see Section 2.4) of the encountered mineral particles. The distribution of orbital solutions suggests prograde orbits.

Table 4. List of relative sensitivity factors (RSFs), used for the calculation of elemental abundances in the mineral particles (Fiege et al. 2014). Values convert from spectral ion abundances to element weight per cent.

Mg	Si	Ca	Cr	Fe
$5.5\ ^{+4}_{-2}$	1	$14.12\ ^{+11}_{-6}$	$5.19\ ^{+4}_{-2}$	$1.32\ ^{+1}_{-0.5}$

also show a clear Si^+ feature. Three mineral spectra are defined by an extraordinarily high iron content (Fig. 3, lower left), that might stem from Fe-rich silicates or Fe-oxides.

To further constrain the compositional variation of the particles, we compare element ratios (main isotopes) inferred from co-added spectra of the four subtypes (Table 3). To ensure the comparability of the method, we only use Mg values where the Na^+/Mg^+ amplitude is dominated by Mg^+. Since, based on the best possible calibration, the Na^+/Mg^+ features in the three Fe-rich spectra appear to be dominated by Na^+, with only minor contribution of Mg^+ at best, the respective $^{56}Fe/^{24}Mg$ and $^{24}Mg/^{28}Si$ ratios are therefore not shown. The elemental abundances were derived after applying relative sensitivity factors (RSFs, Fiege et al. 2014) to the ion abundances of the main isotopes in the spectra, compensating for matrix effects and the ionization efficiencies of different elements (Table 4). From the $^{56}Fe/^{40}Ca$ and $^{56}Fe/^{28}Si$ ratios, the dramatically increased iron abundance in the Fe-rich class is obvious, whereas the other subtypes generally appear to have iron abundances below CI chondritic values. The water/silicate spectra have the highest $^{24}Mg/^{28}Si$ ratios, followed by the Fe-poor silicates. The inferred $^{24}Mg/^{28}Si$ ratio for the high Cr-silicates is on an intermediate level. For the high Cr-silicates, the Cr abundances are significantly enriched relative to Fe, on average the $^{52}Cr/^{56}Fe$ is 0.194, which is a factor of 15 higher than the CI chondrite values (0.013, Lodders 2003). Note, that the presence of Cr in the particles is not a unique interpretation, as the respective mass line in the spectra could also be (partly) due to organics, although this appears to be unlikely (see Section 4.4). Additionally, CDA is only capable of detecting Cr in the particles if it is abundant. Thus, there is a bias towards Cr-rich particles, as CI-typical abundances are below CDA's detection limit and therefore no visible mass line would be present.

Fig. 5 shows Cassini's trajectory during the nine orbital segments that were used for the analysis. The identified mineral grains are highlighted. Although only 27 mineral grains were detected, there is a greater chance of detecting the grains near the ring plane than at higher latitudes. By contrast, detection of water ice particles (Fig. 6), shows that Types 1 and 2 in particular, appear equally distributed over the full analysed range between approximately ± 0.3 R_S, possibly indicative of an isotropic dust background of E ring grains. This implies that mineral grains are on average on less inclined orbits than the icy E ring population. Additionally, we observe that more mineral particles are detected north of the ring plane. The implication of this is investigated in Section 3.3.

3.3 Relative frequencies and spatial distributions

The detection rate of ice grains indicates that ice particles are fairly homogenously distributed over the observed vertical range. The relative frequencies of compositional icy subtypes, however, exhibit stronger variations (Fig. 6, upper panel). The compositional profiles of the five types of dust grains show the highest relative abundance of Type 1 particles to be approximately 80 to 85 per cent. The maximum values for Type 2 and 3 particles are lower, at ∼15 and ∼6 per cent, respectively. Types 2 and 3 also show slight north–south asymmetries, with differences of ∼5 per cent. The asymmetry

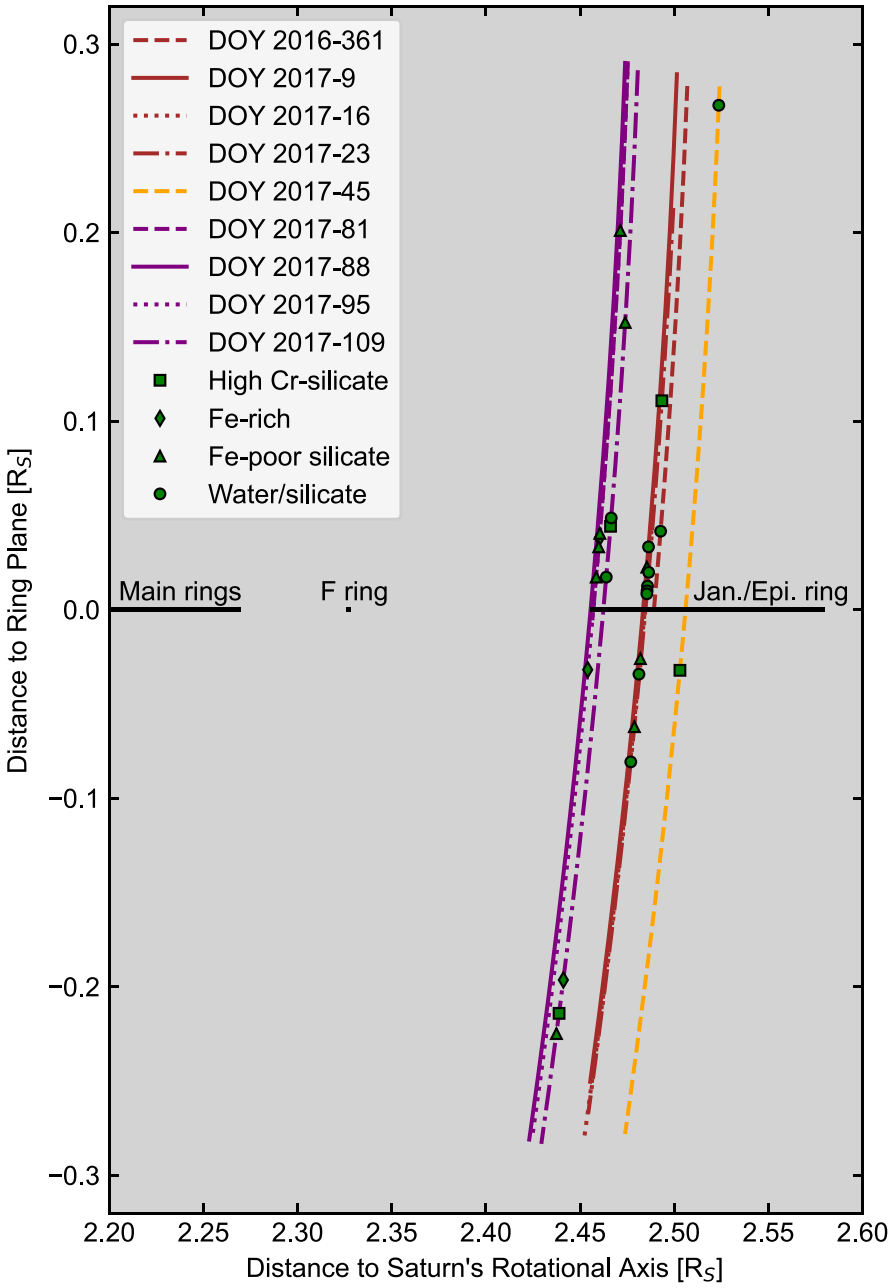

Figure 5. Cross section through the Saturnian system with an overview of the set of RPXs used for the analysis. They are labelled by the DOY when they occurred in 2016 and 2017, respectively. The orbits are divided into three groups (purple, red, and yellow), sorted by the radial distance to the F ring. Encountered mineral dust particles are highlighted in green. Detections of ice particles (Types 1–3 and 5) are distributed along the respective orbits and are shown in Fig. 6 (lower panel). The locations of the shown rings are: Main rings up to ∼2.27 R_S (Porco et al. 1984), F ring at ∼2.33 R_S (Albers et al. 2012), and Janus/Epimetheus ring from ∼2.46 to ∼2.58 R_S (Winter et al. 2018).

in Type 2 grains however turns out not to be statistically significant (see below).

The relative frequencies of Type 4 (mineral dust) and Type 5 particles are the lowest. However, a substantial increase by a factor of approximately three for these particles is observed close to the ring plane, indicating a higher likelihood of detection in this region.

The spatial distribution of the average QI amplitude (ion yield in femtocoulomb), which correlates with the particle mass (Fig. 6, middle panel), differs further. All particle types exhibit increased ion yields around the ring plane, with Types 2 and 4 reaching the highest values of ∼550–650 and ∼700–1100 fC, respectively, whereas Type 1 particles generally exhibit the lowest values. The observed QI values between roughly 2 and 2000 fC are equivalent to particle radii of ∼0.06–0.5 μm, respectively, assuming an impact speed of 20 km s^{-1}. However, this calculation is, as mentioned in Section 2.3, based on a calibration with Fe particles. Therefore, although the sizes for Type 4 particles might be accurate, the water ice dominated particles might be larger, due the potentially lower ion yield of water ice grains. By correcting the ion yield for water ice particles by a factor of 1 to 10 (Hsu et al. 2018), we can still conservatively

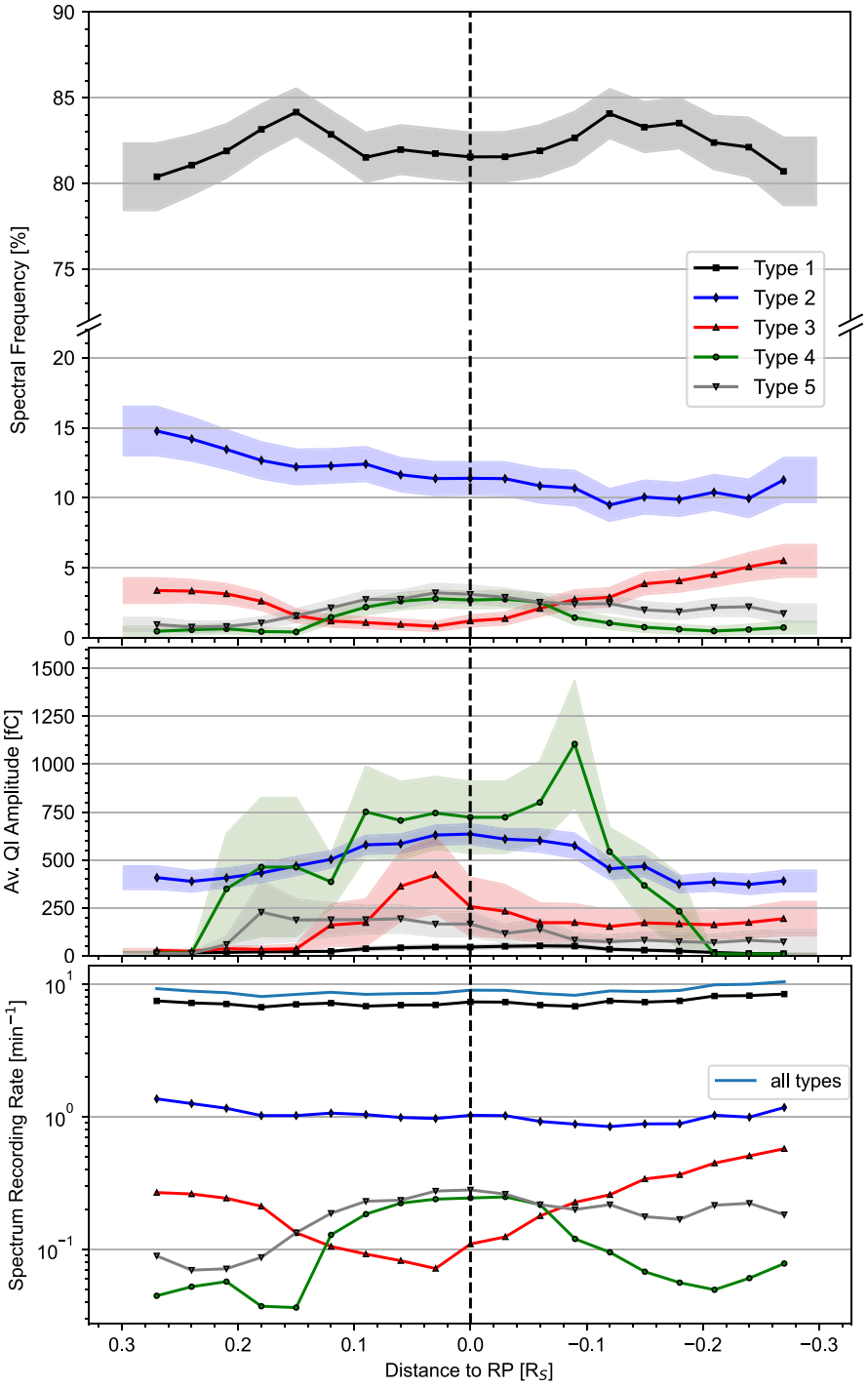

Figure 6. The upper panel shows profiles of the relative compositional frequencies (percentage) of the five detected particle Types 1–5 along Cassini's trajectory during the RGO within ± 0.3 R_S from the ring plane. Over this region, CDA recorded spectra, limited by the instrument's data rate. Therefore, no meaningful number densities could be derived. The middle panel shows the average ion yield (QI amplitude) profiles of these grains in femtocoulomb. The spectrum recording rate (min^{-1}) of the different types is displayed in the lower panel. Error bars reflect the standard error of the mean (SEM), which is defined as $\pm\sqrt{p \times (1-p)/N}$, where p is the relative abundance of particles of a compositional type and N the total number of particles of all compositional types in a particular distance interval (0.2 R_S).

assume particle radii between ∼0.1 and 1 μm for the analysed dust population.

The significance of the north–south asymmetries of Type 4 detections and of the icy types, as shown in Figs 5 and 6, is investigated in Table 5. We apply a hypothesis test (with binomial distribution and a significance level of 95 per cent) to the observed particle detections, assuming that all particles have a 50 per cent chance to be detected either north or south of the ring plane. Due to partial inactivity

Table 5. Hypothesis test of the spatial distribution of the spectral types. The number of particles detected north and south of the ring plane and their expected detection rate (mean value) in case of an equal distribution are shown. Additionally, the inferred range of acceptance for the proposed hypothesis (with a significance level of 95 per cent) and the result of the statistical test are given. The range of acceptance represents the calculated range in which the observed north–south distributions are still in agreement with the assumption of a symmetric distribution.

Spectral type	Detections north of the RP	Detections south of the RP	Range of acceptance (significance of 95 per cent)	Significant asymmetry
Type 1	643	774	672–745	Yes
Type 2	94	85	77–102	No
Type 3	13	31	16–28	Yes
Type 4	14	8	7–15	No
Type 5	13	18	11–20	No

of CDA, the data of DOY 2016–361, 2017–16, and 2017–81 have not been recorded over the entire period relevant for this work and are therefore not considered in this statistical test here. The result shows that the asymmetries have no high significance in the case for detections of Types 2, 4, and 5. The asymmetries in the particle detections of Types 1 and 3, however, are significant. The reason for this is currently unclear and will be further investigated in the future.

Focusing on DOY 45, during which Cassini came closest to the orbits of Janus and Epimetheus, most of the particle impacts produced ion yields below ∼140 fC (Fig. 7). A fraction of the data set (6 per cent) is characterized by distinctly higher ion yields of between 460 and 6700 fC, with an increased frequency of these raised yields close to the ring plane. This is clarified by the middle and lower panels of Fig. 7, that show the number of particles with respect to their ion yield, close to (within $\pm$ 0.1 R_S) and far from (beyond $\pm$ 0.1 R_S) the planets equatorial plane. An interesting aspect of this plot is that within $\pm$ 0.1 R_S of the ring plane, the number of the smallest particles (1–3 fC) appears to decline. This could be related to the dynamics of the smaller size regime that is – in contrast to larger grains – affected by electromagnetic forces (e.g. Hsu et al. 2018) and therefore can be easier dispersed out of the ring plane. Although ion yields above ∼2 pC generally produce unclassifiable spectra, we consider two spectra above this yield limit. Out of the mentioned 6 per cent (12 particles), seven were Type 2, two were Type 1 and one each were Types 3 and 4. One spectrum is too distorted for an explicit type assignment.

3.4 Ionization of target material: the Rh^+ peak

Many mass spectra of the RGO data set show a peak at ∼103 u attributed to Rh^+, which is the material of the CAT (Srama et al. 2004). As described in Section 2.2, dust particles impacting on to the instrument with velocities >8 km s^{-1} are expected to ionize some of the target material and to show a respective Rh^+ mass line in their spectra (Postberg et al. 2009a). The amount of ionized target material depends on different parameters, such as impact velocity, particle mass, and particle density.

In Table 6, the fractions of RGO spectra showing a significant Rh^+ peak (>2 Sigma from the local noise level) are listed. There, a clear compositional dependence can be observed. Almost all Types 2 and 4 spectra – 94.5 and 96.3 per cent, respectively – exhibit a Rh^+ mass line. Those who do not show a Rh^+ signal show a general low signal to noise and low total ion yield.

The salt-rich Type 3 and 5 spectra exhibit the lowest fractions, with 11.8 and 14.6 per cent, respectively. Although Type 1 particles have much smaller ion yields than Types 3 and 5 (Fig. 6), they produce more (49.5 per cent) and higher Rh^+ peaks. Type 2 ice particles are generally larger than Type 1 grains (Khawaja et al. 2019; Nölle et al. 2024; Ershova et al., in preparation) and are therefore expected to excavate and ionize large amounts of the target material. Co-added spectra of the five compositional types are shown in the supplementary material (Fig. S2). We discuss the implication of these differences in Section 4.2.

4 DISCUSSION

Here, we discuss the implications of the presented analysis, starting with the water ice dominated species and their indication for the extension of the E ring (Section 4.1), followed by a closer elaboration on the salt-bearing particles (Section 4.2). We examine the influence of the Janus/Epimetheus ring on the sampled region (Section 4.3) and the compositional and dynamical aspects of the mineral fraction that in turn can be used to discuss their potential sources (Sections 4.4 and 4.5).

4.1 Water-dominated ice grains (Types 1, 2, 3, and 5), an inner extension of the E ring

The CDA spectra of ice grains recorded during the RGO comprise the same compositional types as reported for the Enceladean ice particles in the E ring (Hillier et al. 2007; Postberg et al. 2008; Khawaja et al. 2019; Nölle et al. 2024). In particular, the presence of salt-bearing Type 3 ice particles (Postberg et al. 2009b) in the RGO data suggests that the orbits of E ring particles are reshaped by dynamical effects (e.g. plasma drag, radiation pressure or Lorentz forces) to venture within the orbit of Mimas (3.07 R_S). Observations from Earth show that the E ring extends inwards to at least 3.07 R_S (Kempf et al. 2018) with photometric observations of Janus' surface colouration also in agreement with E ring material deposition (Verbiscer et al. 2007, 2018). More sensitive Cassini remote sensing observations confirm the extension to smaller Saturn radii (e.g. Hedman et al. (2012) show an E ring extension south of Saturn's equatorial plane to as far as the G ring, potentially even as far as the Janus/Epimetheus ring). Hedman et al. (2020) have also detected surface brightness variations on Janus and Epimetheus, consistent with E ring grain deposition on the moons' trailing sides. The ability of E ring grains to reach this far (e.g. to within 2 R_S of Saturn) has been shown through modelling, but only for grains with radii larger than 0.5 μm (Horányi, Juhász & Morfill 2008). CDA is sensitive to much smaller grains, and here we show that smaller E ring grains with radii below 0.5 μm migrate inwards to 2.45 R_S, possibly reaching the outer edges of the A ring.

During the Cassini mission, most spectra generated by E ring particles were from impacts at speeds below ∼12 km s^{-1}. The E ring spectra chosen for the spectral comparison with the RGO spectra (Fig. 2) represent those with the highest impact speeds (15–18 km s^{-1}) and therefore are comparable to the spectra recorded during

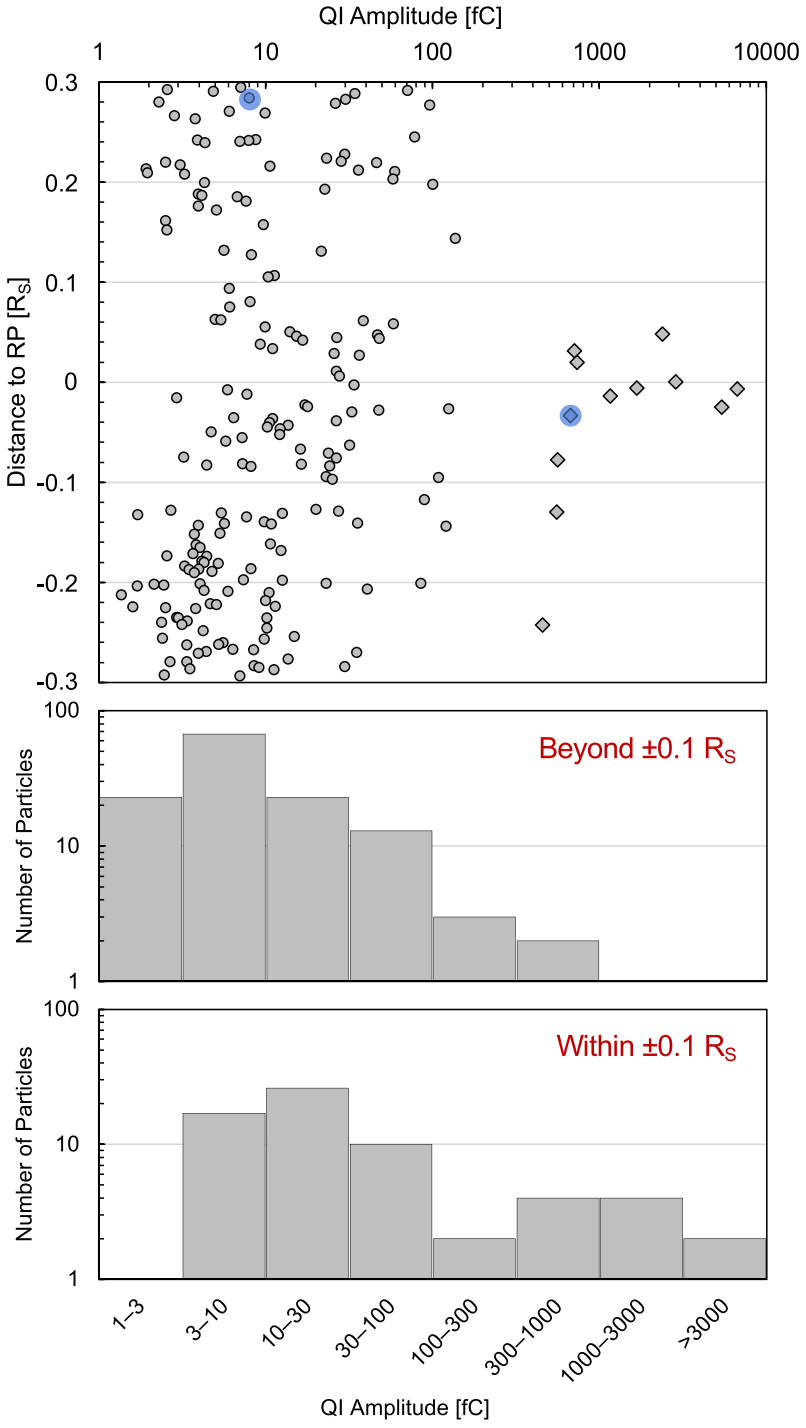

Figure 7. Ion yield (QI amplitude in femtocoulomb) of the individual particles detected during DOY 2017–45. The two identified mineral particles are highlighted in blue. The particles with QI amplitudes > 300 fC (diamond symbols) show a clear separation from the bulk population (grey circles) and might represent material from the Janus/Epimetheus ring. 58 per cent of them are of Type 2. The middle and lower panels display the number of particles with respect to the ion yield, both beyond and within ± 0.1 R_S.

Table 6. Fraction of the respective spectral types with Rh^+ peaks.

Spectral type	Type 1	Type 2	Type 3	Type 4	Type 5
Rh^+ peak (per cent)	49.5	94.5	11.8	96.3	14.6

the RGO (19–21 km s^{-1}). At impact speeds <10 km s^{-1}, mass spectral peaks are mostly due to molecular ions, as well as water clusters. At impact speeds >15 km s^{-1}, molecular ions and water clusters are to a greater part dissociated, and hence their spectral features become weaker or disappear entirely (Postberg et al. 2011). Similarly, during the RGO, at impact speeds of approximately 20 km

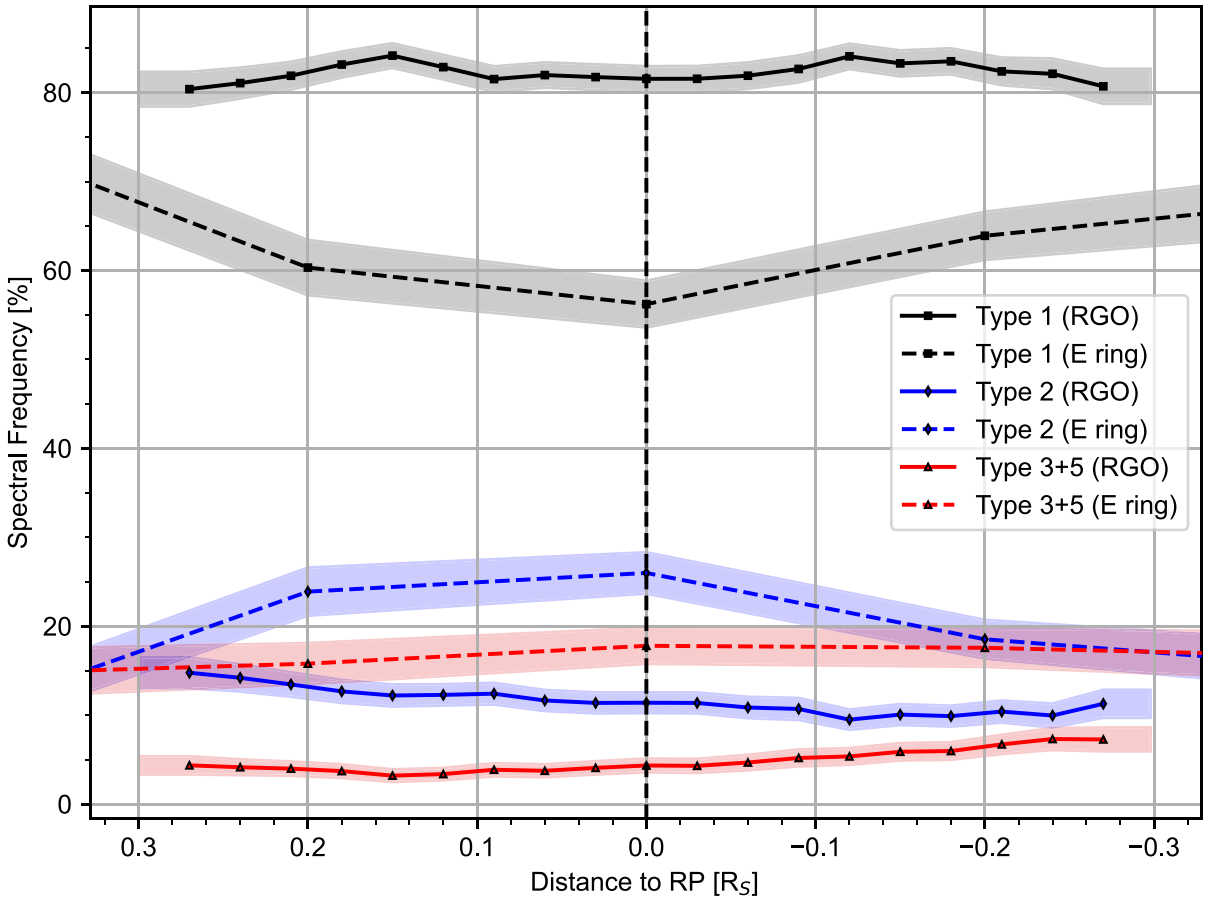

Figure 8. Comparison of the merged RGO data with the vertical profile through the central E ring at radial distances of 4.3–5 R_S. Type 1 clearly dominates in both profiles, with Types 2 and 3 showing comparable trends although their relative abundances are higher in the E ring. Type 1 drops to less than 60 per cent at the ring plane in the E ring, whereas Type 2 shows a maximum (26 per cent) in this region. Type 4 is not shown here, as these particles are dynamically not part of the E ring (Trieloff et al. 2023). Error bars are calculated as in Fig. 6.

s^{-1}, significant fragmentation of molecular species from the ice grains can be observed in the spectra.

In Fig. 8, we compare the proportions of the ice grain compositional Types 1–3 and 5, as seen during these RGO, with vertical profiles of grains detected in the central E ring (4.3–5 R_S, Table S2). Note, that the Type 3 and Type 5 profiles are combined, as the latter particle type is rarely detected in this specific region of the E ring (Nölle et al. 2024, a detailed investigation of these two salt-rich types follows in Section 4.2). Pure water ice grains (Type 1) are the dominating compositional type in both the central E ring and the RGO profiles. However, their relative abundance in the RGO profile is ∼80 per cent, so clearly higher than seen in the central E ring profile through the equatorial plane (∼60 per cent). In contrast, the maximum relative abundance of Type 2 grains in the central E ring is ∼25 per cent at the ring plane, compared to ∼10–15 per cent during the RGO, without any indication for an enrichment towards the ring plane. In case of salt-rich particles, the combined relative abundance of Types 3 and 5 in the central E ring is ∼15–20 per cent during the entire profile, whereas it is ∼5 per cent for the RGO data set. Salt-containing particles are therefore found to be more abundant in the central E ring than in the RGO, with an indication of a slight enrichment below the ring plane in both cases.

One potential explanation for the differences in the particle properties between the central E ring and the RGO is an observational bias, i.e. that CDA observed much smaller grains during the RGO. CDA can only produce interpretable spectra within a relatively narrow range of QI ion yield, approximately 2–2000 fC. The strong dependence of ion yield on impact speed (see equation 1 in Section 2.3) means that different impact speeds result in the investigation of different size regimes if the QI ion yields are the same. Thus, E ring particles (detected at relative velocities of ∼8 km s^{-1}) will be larger, by a factor of approximately four, than particles detected during the RGO (20 km s^{-1}). The observed size regimes of the RGO population and the E ring reference population are therefore unlikely to overlap. The domination of Type 1 in the RGO profile agrees well with the assumption that Type 2 grains are systematically larger than Type 1 grains (Khawaja et al. 2019; Ershova et al., in preparation) and therefore Type 1 grains become more abundant in the CDA size window of the RGO. Also the reduced proportion of Type 3 – compared to both the central and the outer E ring – may be related to the relatively higher impact speeds onto the instrument during the RGO in two ways. Firstly, the fraction of Type 3 grains is indeed expected to become smaller compared to Type 1 grains in the observed smaller RGO size regime (Postberg et al. 2011; Ershova et al., in preparation). Secondly, molecular cluster peaks such as $[Na(NaOH)]^+$ at 63 u (Section 2.2) might not always be stable upon such high speed impacts of the particles, resulting in single peak spectra, with only Na^+ mass lines, that are often

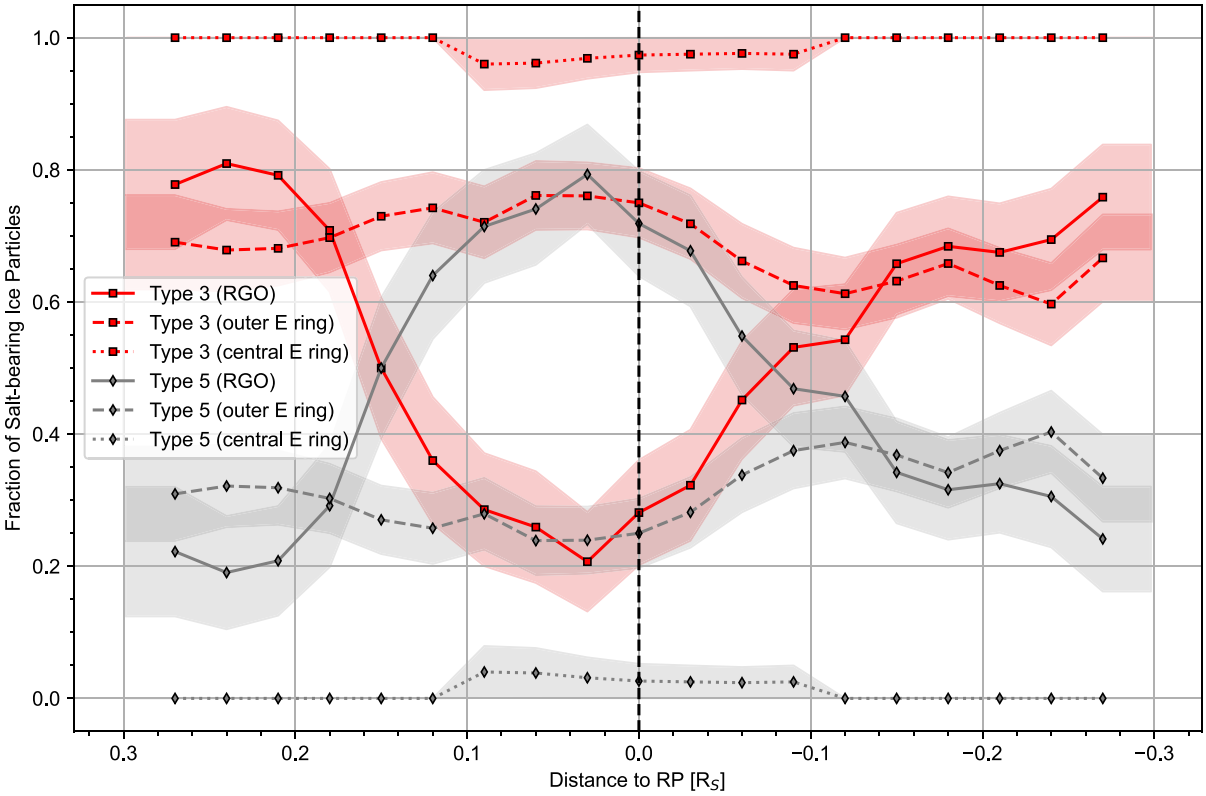

Figure 9. The spectral fractions of Types 3 and 5 near the F ring compared to observations in both the central (4.3–5 R_S, Table S2) and outer (∼8.7–8.8 R_S, Table S2) E ring, within the same vertical distances from the ring plane. Please note that the combined fraction of salt-rich grains (Types 3 and 5 combined, Fig. 8) observed during the RGO is lower than anywhere in the E ring. The fractions are defined as $\boldsymbol{n_{Type\_i}}/(\boldsymbol{n_{Type\_3}} + \boldsymbol{n_{Type\_5}})$, where $n_{\mathrm{Type\_i}}$ is the number of particles of the respective type per distance interval of 0.2 R_S. Error bars are calculated as in Fig. 6.

discarded by the CDA onboard software before transmission to Earth.

Another process that could produce the enrichment of Type 1 over Type 2 grains is radiation-driven photochemical alteration. Nölle et al. (2024) examined this process, through which organic species were volatilised and removed from Type 2 grains, effectively turning their composition into Type 1, with a concomitant size reduction as both volatiles (and water) were also removed by plasma sputtering. Indeed, Nölle et al. (2024) found a similar enrichment of Type 1 versus Type 2 in the outer E ring (outwards of about 8 R_S, see fig. 7 in Nölle et al. 2024) as that found in grains sampled during the RGO. The time taken to change the orbital elements of ice grains ejected by Enceladus into the E ring, in such a way that they can reach the regions we sampled during the RGO, might be sufficient to make this space weathering process as significant in altering the grains' compositions as found by Nölle et al. (2024) for grains evolving outward from Enceladus. It is important to note that particles reaching inwards of Mimas orbit need to have high eccentricities. It is therefore possible that the apokrone of ice grains that we observe here at their perikrone, lies at a distance of 8 R_S or outwards. Thus, it might indeed be viable that there is a substantial overlap in the E ring dust populations observed here and outward of 8 R_S.

4.2 Salt-bearing particles – Types 3 and 5

In the central E ring (CDA data taken from 4.3 to 5 R_S; Table S2) Type 3 clearly dominates, whereas Type 5 is essentially insignificant. Enceladus injects fresh Type 3 grains into this region and only few space-weathered Type 5 grains reside here. The outer E ring profile (recorded between approximately 8.7 and 8.8 R_S, Table S2), however, agrees very well with the average RGO proportions. On average it takes decades to centuries for grains to be moved by plasma drag from the vicinity of Enceladus to the outer E ring (Dikarev & Krivov 1998), which will turn a substantial fraction of Type 3 grains into Type 5 grains (Nölle et al. 2024). Our RGO observations indicate that it therefore takes a similar time for the perikrones of these E ring grain orbits to evolve below 2.5 R_S.

The relative abundances of Type 3 and 5 particles along the vertical profile of the RGO show opposing trends (Fig. 6). Type 5 is more frequent close to the ring plane, whereas Type 3 dominates at higher latitudes. To investigate the increased likelihood of detection of Type 5 grains in the ring plane, we compare the ratios of the two salt-bearing types along the vertical RGO profile with those recorded in the central and the outer E ring (Fig. 9). Our data suggest a currently unknown process that increases the probability for Type 5 to be detected near the ring plane, an effect comparable to that seen for the mineral grains (Fig. 6). There is no indication that Type 5 particles become more abundant towards the orbits of Janus and Epimetheus, lowering the probability for a moon origin. Thus, an E ring origin appears to be more likely, with the aforementioned aging effect of Type 3 grains as a potential production mechanism (Nölle et al. 2024). Dynamically one would expect larger grains to acquire higher inclinations slower than smaller grains, and thus generally larger grains accumulate near the ring plane (e.g. Kempf et al. 2008). However, Type 5 grains are generally smaller than

their progenitor Type 3 grains (Fig. 6), a result of the erosion of water ice from these grains and also observed in the E ring data (Nölle et al. 2024). Thus, it remains currently unclear why we have such a pronounced accumulation of very salt-rich Type 5 grains near the ring plane, not seen at other locations in the E ring, at ∼2.45 R_S.

Another interesting aspect of the salt-bearing particles is that their spectra all exhibit extraordinarily weak Rh^+ mass lines from CDA's target material. The presence of Rh^+ mass lines in the spectra depends on different parameters (see Section 3.4) and may in this case be relevant to understanding the microstructure of the attributed grains. Despite having a higher ion yield than Type 1 (Fig. 6), much smaller fractions of Type 3 and Type 5 spectra (11.8 and 14.6 per cent compared to 49.5 per cent in Type 1) have Rh^+ mass lines (see Table 6).

Although these salty types have somewhat higher ionization efficiencies than pure ice of Type 1 (Nölle et al. 2024), this does not compensate the much higher overall measured ion yields (Fig. 6). Type 1 grains are therefore on average smaller than those of Types 3 and 5. Since smaller mass cannot account for the smaller amounts of target material rhodium seen in the spectra of salt-rich ices, this implies possible structural differences among the compositional particle types. It is known that 'fluffy' dust particle analogues produce less impact charge than compact particles of the same composition, which potentially has an influence on the ionization of target material (Hunziker et al. 2022). Postberg et al. (2009a) reports an increase of the impact velocity threshold for the appearance of Rh^+ in CDA spectra with decreasing density of the impinging particle (table 4 in Postberg et al. 2009a). Similarly, the salt-rich particles of our study could be less compact than salt-poor species, producing less ionized target material during impact on to the instrument.

Additionally, suppression effects from salts in a water-rich matrix on the spectral appearance are observed in analogue experiments (Napoleoni et al. 2023a,b). High-salt concentration suppresses ionization of other species. Thus, a second reasonable explanation for the low abundance of Rh^+ peaks might be that high salt content in the particles suppresses the formation of Rh^+ ions. This last factor is particularly relevant for Type 5 grains, which shows no other mass lines other than Na^+ and K^+, an indicator of strong suppression effects. Since the presence of Rh^+ ions is even rarer in spectra of the less saltier Type 3 grains (Table 6), suppression effects alone cannot account for this there. Therefore, structural/physical differences, like the aforementioned reduced density, have to play an additional role for Type 3 grains.

4.3 Janus/Epimetheus ring

During DOY 2017–45, Cassini came closer than ever to the orbits of Janus and Epimetheus, enabling CDA to sample the denser part of the tenuous Janus/Epimetheus ring, made of moon impact ejecta that evolves from Janus and Epimetheus after being lifted from the moons' surfaces by the hypervelocity impacts of micrometeoroids (Krüger et al. 1999; Seiß et al. 2017; Buratti et al. 2019). The twelve dust particles mentioned above (diamond symbols in Fig. 7) do not follow the size distribution of the E ring background at this outermost location of the RGO and are closely confined to the ring plane within ±0.1 R_S. Faster impact speeds on to the instrument, e.g. resulting from particles on inclined orbits, would also increase the ion yields, however, since most of these particles are confined to the ring plane and have been observed with identical instrument pointing, there is no indication that orbital elements of these dust grains are very different from the other dust grains observed during this orbit. We note that even if this is the case, it would still signify an additional dust population on top of the E ring background, distinguished not only by mass but also by orbital dynamics. Thus, the most plausible explanation is an origin from the Janus/Epimetheus ring rather than the E ring, although this is not a unique interpretation.

This would agree with CDA-HRD observations described in Buratti et al. (2019), which found that the density of grains with radii ≥1.6 μm increased by roughly a factor of two in the vicinity of the orbits of Janus and Epimetheus over a characteristic scale length of 3500 km, while the density of smaller grains did not change. Thus, the bigger particles stay closer to their parent bodies, as they are less affected by nongravitational forces (Buratti et al. 2019). This also agrees with findings from other passes through the Janus/Epimetheus ring with greater distances to the moons' orbits (DOY 2017–81, 88, 95, and 109), where the fractions of larger grains relative to the bulk dust populations are significantly smaller when compared to the observations of DOY 2017–45 (Fig. 7). Ye et al. (2018) present Cassini RPWS measurements of the Janus/Epimetheus ring. There, the thickness (FWHM) of the ring is estimated to vary between 600 and 1000 km, depending on the distance to the moons' orbits. This is less than the vertical distribution of our twelve particles relative to the ring plane (Fig. 7). However, since Ye et al. (2018) consider a size threshold of 1 μm for the ring particles, the probably smaller (sub-μm) particles measured with CDA, could reach higher latitudes.

Ten of the twelve potential Janus/Epimetheus ring particles are icy. One salt-rich ice particle, two pure water ice particles, seven organic-bearing ice grains, and one non-icy high Cr-silicate particle could be identified. The high ion yields from the large particles detected lie at and above the upper charge limit of the CDA Chemical Analyser subsystem (typically corresponding to a maximum QI amplitude of about 2000 fC) and therefore one of the spectra with an ion yield of 5400 fC is too distorted for a reliable compositional interpretation. A high relative abundance of Type 2 particles in this subset of large grains is expected, as Type 2 generally exhibit the highest QI amplitudes of all icy grain types (Fig. 6, Khawaja et al. 2019; Ershova et al., in preparation). Thus, they are the dominant particle type in this larger size regime. The observed Type 2 spectra and the other icy dust particles of this subsample show no compositional differences to generic Type 1, 2, and 3 spectra from the E ring (Fig. 2). Thus, although not fitting into the size distribution of the E ring background, they are compositionally indistinguishable from it. The only exception is the one mineral dust grain in the subsample.

Since the most likely source for these large grains are the surfaces of Janus and Epimetheus, we infer that the surfaces of the moons are coated with E ring dust, with possible addition from silicates and other minerals, and also icy particles collected by the moons from the main rings or various external sources. The impact ejection as production mechanism for the particles populating the Janus/Epimetheus ring typically produces less steep size distributions (Krüger et al. 1999; Koschny & Grün 2001), compared to those found for the E ring population (Kempf et al. 2008, 2010, 2018). In this region both distributions seem to overlap and only its high-mass tail together with its tentative better confinement to the ring plane makes the Janus/Epimetheus ring noticeable in our data. Thus, many smaller water ice particles that were detected in the same regions could stem from the moons, however there are no compositional means, except perhaps the occasional presence of silicates, by which moon or E ring material could be distinguished. In addition, it is likely that the larger ejecta do not reflect individual E ring grains, but rather show mixed compositions comprised of material stemming from both the

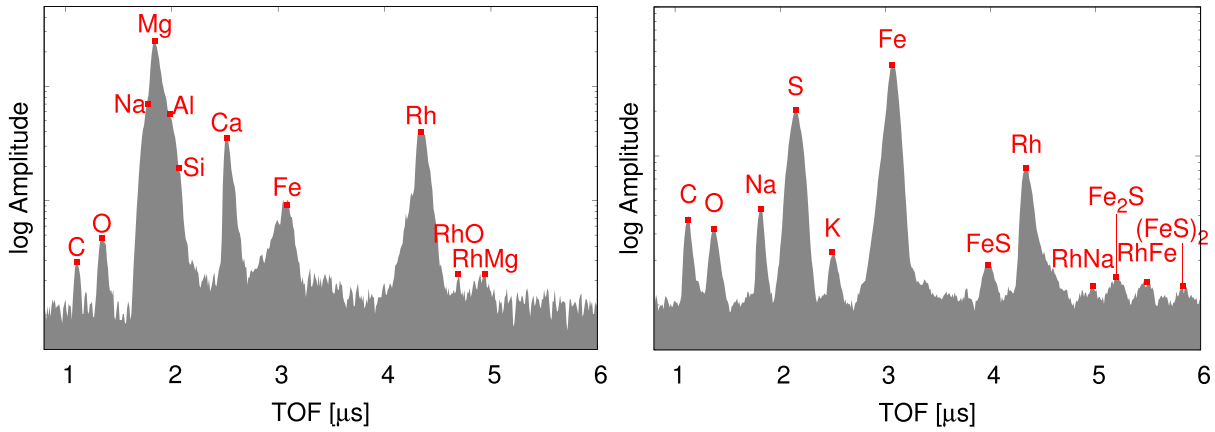

Figure 10. Typical example spectra of mineral grains detected in the Saturnian system during Cassini's orbital tour, with Mg-rich siliceous (left) and Fe-rich (right) compositions. The Fe-rich spectrum is attributed to iron sulfide, which is the most abundant Fe-rich subtype (Fischer et al. 2018).

E ring and other external sources that accumulated on the moons' surfaces.

The surface composition of Janus and Epimetheus was investigated with Cassini's Visible and Infrared Mapping Spectrometer (VIMS; Brown et al. 2004). Bluer colours in the VIMS spectra indicate a composition closer to pure water ice, while redder colours indicate a higher amount of a chromophore that may come from the main rings (Buratti et al. 2019). This interpretation is based on the observation that moons become less red with increasing distance from the main rings. Epimetheus' colour is already comparable to the colours of Enceladus and Mimas, implying effective E ring deposition. Janus' colour, however, is distinct from those of Enceladus and Mimas (Filacchione et al. 2013), arguing for additional contaminants, potentially organic- or iron-rich grains from the main rings (Cuzzi et al. 2009). Therefore, organic particles from the inner Saturnian system could also be a contributor to the dust population measured during the RGO. Although the analysed RGO Type 2 spectra are in good agreement with those of generic E ring grains, there are currently no compositional constraints to rule out a potential influence of an additional source. This is due to the high impact speeds during the RGO and also during the subsequent Grand Finale orbits (where confirmed debris from the main rings was sampled, e.g. Hsu et al. 2018), that removed detailed information about the organic constituents in the particles. Linti et al. (2024) investigate the compositions of mineral grains ejected from the main rings, the composition of icy grains, however, will be subject of a future paper. The differing colour of Janus could also be explained by the presence of space weathered E ring particles on Janus' surface, the compositions of which are altered by loss of water ice or photochemistry, potentially already during the inward transport from the E ring (Nölle et al. 2024) and more severe after being deposited on to the moon's surface. Smaller ring shepherd moons like Atlas and Pan are less red than their surrounding rings, and therefore E ring particles might also play a role here, preferably on the leading hemispheres of the moons (Buratti, Mosher & Johnson 1990; Hamilton & Burns 1994; Verbiscer et al. 2007; Kempf et al. 2018). These observations also support our findings and indeed suggests that E ring particles reach the region between the F ring and the co-orbital moons, and that the impact ejecta forming the ring along Janus' and Epimetheus' orbits could, at least to a greater part, be formed from E ring material previously deposited on the moons, overlapping with fresh E ring material in this region.

4.4 Mineral grains – composition and origin

Over a period of 13 yr, Cassini encountered several types of mineral particles in the Saturnian system. These particles can be assigned to either ISD grains (Altobelli et al. 2016) or other interplanetary dust particles (IDP): some endogenous to the Saturnian system, others sun-bound exogenous particles crossing the Saturnian system (Trieloff et al. 2023). A further important group of mineral grains is the main ring debris that falls into Saturn and was sampled during the Grand Finale orbits (Hsu et al. 2018; Linti et al. 2024). We now compare the compositions of the RGO mineral grains (Fig. 3) with those of the different mineral populations encountered by CDA.

The ISD particles were identified by their dynamics and composition. From their mass spectra they are inferred to be mostly Mg-rich silicates or oxides. The main mineral-forming elements (Mg, Si, Ca, and Fe) appear at about CI chondritic abundances and are in agreement with relatively homogenous compositions rather than e.g. specific minerals (Altobelli et al. 2016). The much larger number of mineral IDP spectra detected during Cassini's orbital tour can be categorized in two major classes: Mg-rich silicates and Fe-rich particles, which are mostly sulfides (Fig. 10; Fischer et al. 2018). However, although detected mostly in the E ring region owing to the large amount of time Cassini spent here), these are either on retrograde orbits or – as mentioned above – traverse the Saturnian system on hyperbolic trajectories (Trieloff et al. 2023) and thus represent a different dynamical population in comparison to both E ring grains and, as we have shown above, the prograde mineral grains observed during the RGO.

In the IDP population (more than 1000 detections), Fischer et al. (2018) observe ∼54 per cent Fe-sulfides, indicated by a strong S^+ mass line in addition to a molecular FeS^+ mass line (88 u) at ∼4 µs (Fig. 10, right). Interestingly, this most abundant compositional type in Saturn's IDP population is not observed in the RGO data. By contrast, the three Fe-rich spectra in this work are in good agreement with Fe-oxide dominated compositions, such as hematite, with much smaller amounts of silicates, a type which is generally rare in the IDP population sampled by CDA (Fischer et al. 2018). However, noting the small number statistics involved, with only three spectra of this Fe-rich mineral type were identified in the RGO data set, it is worth discussing the implications of the measurements.

Earlier studies (Clark et al. 2008, 2012; Cuzzi et al. 2009) discuss nanophase hematite as a possible UV absorber spread over the Saturnian system, such as on the surface of Dione or in Saturn's rings,

albeit with no known source. The three Fe-rich grains (Fig. 3, lower left) detected during the RGO might represent such grains. Since Fe-oxide grains are very rare in the CDA measured IDP population (Fischer et al. 2018), it is more likely that these grains originate from a nearby source (e.g. the F ring, the moons, or the main rings).

However, CDA did not detect any Fe-rich grains in the population originating from the main rings and falling into Saturn (Linti et al. 2024) during the RPXs of the subsequent Grand Finale orbits. This main ring debris is exclusively made of silicates characterized by a low Fe content and Mg, Si and Ca in roughly CI chondritic abundances (Linti et al. 2024). Grains with similar compositions were also detected during the RGO, and we consider it likely that the Fe-poor silicates presented in this work also have their origins in the main rings (Section 4.5).

In contrast to the ISD observed by CDA, which supposedly was subject to homogenization processes in the interstellar medium (Altobelli et al. 2016), only a few of the element ratios inferred from the RGO mineral spectra (Table 3) agree with CI chondritic values. There could be several reasons for this discrepancy: (i) unlike chondrites, the detected RGO particles, with small sizes in the order of a few 100s of nm, are most likely not multi-mineral phases, thus a deviation from a bulk chondritic composition is expected. Even if the particles would consist of different mineral phases, they would not be expected to be present in the exact same fractions as e.g. in chondrites; (ii) most of the silicate particles are depleted in Fe, similar to the silicates stemming from the main rings (Linti et al. 2024), leading to significant deviations from CI chondritic abundances; and (iii) measured Mg and Ca abundances might be significantly affected by neighbouring mass lines from instrument target contaminants (Na and K), resulting in an unquantifiable overestimation of the two elements. Although Na and K could also stem from the particles as well, a certain level of contamination is expected, after target contamination by the large amounts of salty ice grains that hit the instrument during more than 20 traversals through Enceladus' plume prior to the RGO (Hsu et al. 2018). However, the inferred element ratios appear to represent realistic values, as almost all individual $^{56}Fe/^{24}Mg$, $^{56}Fe/^{28}Si$, and $^{24}Mg/^{28}Si$ ratios are in the range of e.g. Fe-rich and Mg-rich olivine, which implies the Na (and K) contamination is not a significant factor affecting the quantification of Mg (and Ca) in the RGO data set.

Additionally, it is in principle possible that the peak we identify as Cr^+ at about 52 u in the high Cr-silicate spectra (Fig. 3, top right) could also stem from cations of C_4-hydrocarbons ($C_4H_{3\text{-}5}{}^+$). At these impact speeds this would however inevitably create larger amounts of C_3- and C_2-fragments, which would appear at around 40 u ($C_3H_{3\text{–}5}{}^+$) and 28 u ($C_2H_{3\text{–}5}{}^+$), respectively. The high amplitude of the peak at 28 u we attributed to Si^+ indeed seems to be in agreement with this interpretation. However, the 40 u peak we attributed to Ca^+ shows no particularly high amplitudes compared to the other mineral subtypes, limiting the possible contibution from C_3-fragments in the potentially high Cr-silicate spectra. Therefore, we do not consider a contribution from organics to be important in this subtype as well as in the other mineral grains detected during the RGO.

Unlike the known mineral dust populations mentioned above, the mineral particles detected during the RGO show a much wider compositional range in a relatively small sample, suggesting different particle sources. The relative frequency of mineral particles increases compared to water ice grains in the ring plane (Fig. 6), independent of their exact composition. Dynamical analysis, based on the possible solutions for eccentricity and inclination, shows that all detected mineral particles were on prograde orbits around Saturn (Fig. 4). Therefore, the mineral grains cannot be distinguished dynamically from the icy population encountered during the RGO. This contrasts with the findings regarding mineral grains detected during E ring passages, where encountered mineral grains were either on retrograde orbits or from sources outside the Saturnian system (Altobelli et al. 2016; Fischer et al. 2018; Trieloff et al. 2023), implying that the mineral grains sampled during the RGO have an entirely different, prograde source.

Agreeing with the dynamical difference, only one-third of the mineral particles detected in this work are similar to previously analysed mineral particles found elsewhere in the Saturnian system. With the exception of a single Cr-bearing exogenous ISD grain (Altobelli et al. 2016), the high Cr-silicate and water/silicate mixed grains, which together account for over half the mineral particles in the RGO mineral grain dataset, have not been detected elsewhere in the Saturnian system by CDA. Together with the derived prograde particle dynamics (Fig. 4), this again suggests a completely independent population with a nearby source.

Since the E ring consists entirely of icy grains, plausible sources for those mineral grains could be either the F ring, the G ring, the nearby moons Pandora, Janus and Epimetheus (Seiß et al. 2017; Buratti et al. 2019), the main rings or a combination of all of them. The water/silicate mixed phases (Fig. 3, lower right) in particular, require recent formation either in the F ring or the nearby moons, because such small amounts of water ice in submicron sized grains are expected to be lost by sputtering and sublimation within a few years (Jurac et al. 2001a; Johnson et al. 2008). Since Cassini travelled through the faint Janus/Epimetheus ring during all RGO with RPXs closer to the orbits of Janus and Epimetheus than to the F ring (Fig. 5) and these moons have been previously identified as a dust source (Williams & Murray 2011; Seiß et al. 2017; Buratti et al. 2019), this means there is a high probability that these unique mineral particles stem from the moons. However, if the moons are their original source(s), or if they stem from interplanetary dust particle (IDP) impact gardening on the moons' surfaces, remains unclear. There are, however, strong arguments for a significant contribution from silicate ejecta from the main rings, which is discussed in the following section.

4.5 Ejecta from the main rings

During the subsequent Grand Finale orbits, CDA detected nanodust grains, which mostly originated from the main rings (Hsu et al. 2018). The mineral grains of this ring material consist exclusively of Fe-poor silicates, with only a moderate elemental variation (Linti et al. 2024). With a fractional abundance of mineral grains of ∼30 per cent of all grains detected ± 20 min with respect to the ring plane crossings, this ring particle data set, however, has a significantly higher fraction of mineral grains than the ∼1 per cent observed during the RGO.

As 33 per cent of these mineral grains detected during the RGO can also be assigned as Fe-poor silicates, a main ring origin for this fraction of mineral grains seems plausible. However, the much lower ion yields of the main ring silicates detected during the Grand Finale orbits indicate radii mostly between 20 and 100 nm (Linti et al. 2024), on average several times less massive than the Fe-poor mineral grains observed here. Therefore, during the Grand Finale orbits debris from the main rings was dynamically strongly affected by electromagnetic forces (Northrop & Hill 1982) due to their higher charge to mass ratio. Hsu et al. (2018) concluded that their sample mostly stemmed from the C and B rings. The larger grains in this study lead to the assumption that electromagnetic forces are negligible and gravitation dominates the particle dynamics, and thus nearby rings are more likely to be potential sources. During the

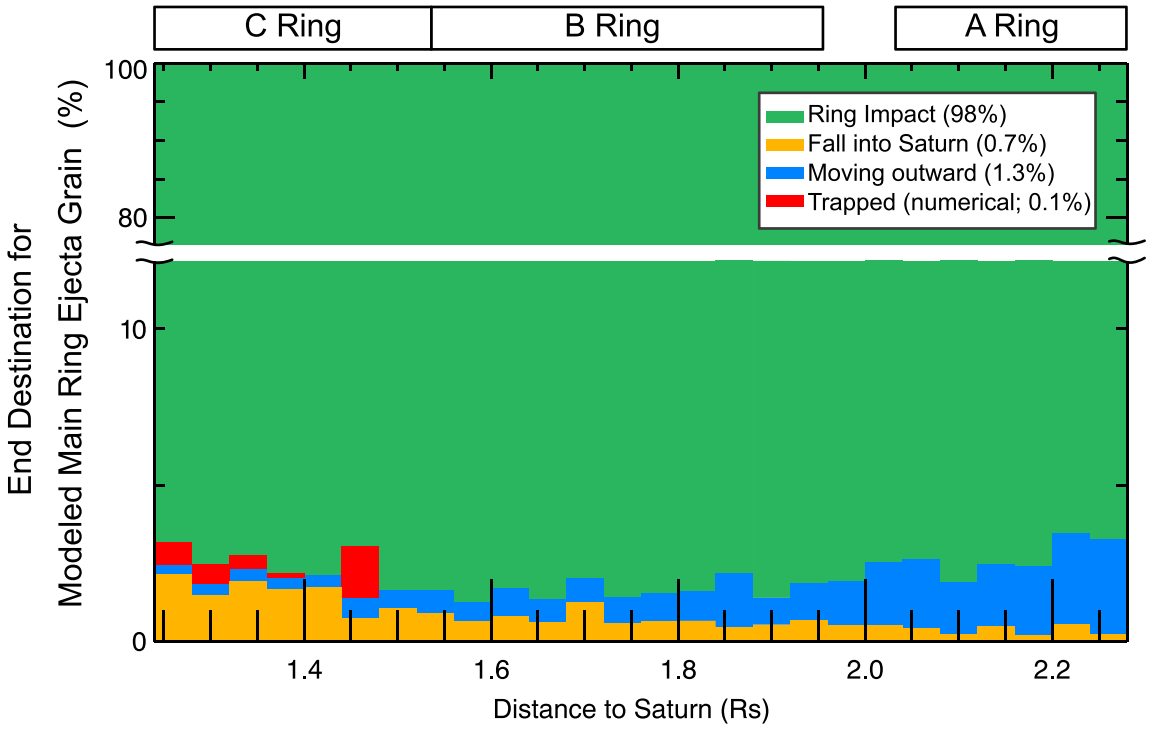

Figure 11. End of simulation for modelled main ring ejecta grains. The grain radii are assumed to be 90 nm to be comparable with the detections reported in this work. Most grains recollide with the rings (98 per cent, green), whereas only 2 per cent escape from the rings either towards Saturn (0.7 per cent, yellow) or move outwards beyond 2.5 R_S (1.3 per cent, blue). This indicates that the main ring ejecta could contribute to the detections near the Janus/Epimetheus orbits. A small fraction (0.1 per cent, red) is trapped at the end of the simulation, from which most can be assumed to recollide with the rings.

RGO a different region of the main rings, presumably the outer ring segments, might therefore have been probed. Following a similar modelling approach to that previously applied (Hsu et al. 2018), we model the dynamical evolution of main ring ejecta assumed to be lifted by micrometeoroid impacts (Fig. 11). We consider grains 90 nm in radii emitted from the rings, with a flux depending on the rings' optical depth profiles, surface areas, and radial distance (for gravitational focusing of the impactor flux). Grains are assumed to be impact ejecta and are launched from the ring plane with a speed up to 10 km s^{-1} following a modified power law with a slope of –1 above 1 km s^{-1}, in addition to the local circular Keplerian orbital velocity (see Hsu et al. 2018). Saturn's gravitational field (up to J2 term) and the magnetic field (Z3 model) were used to calculate the grains' dynamical evolution. Grain charging is simultaneously modelled based on an ad hoc plasma model (Hsu et al. 2018), although the effect of the charging and thus the Lorentz force is expected to be minimal, given the overall low charge-to-mass ratio for 90 nm-sized grains. Each simulation ends when the modelled grain either (i) recollides with the rings – 98 per cent, (ii) falls into Saturn – 0.7 per cent, (iii) moves outwards and reaches 2.5 R_S – 1.3 per cent, or (iv) remains aloft after 360 h – 0.1 per cent. The model results (Fig. 11) predict that a small fraction (1.3 per cent) of the ejected main ring material – mostly from the A ring – moves outwards over 2.5 R_S and may be detected near the Janus/Epimetheus orbits. With the initial conditions used for the simulation, these ring ejecta moving outside of the ring also show a higher concentration within ±0.1 R_S from the ring plane. Therefore, a contribution from the main rings in the observed size range is indeed possible and may be responsible for the Fe-poor silicate subgroup seen during the RGO. The main ring contribution, however, is likely only a minor contribution compared to the Janus/Epimetheus ring, given the discontinuity between the Janus/Epimetheus ring and the main rings seen in the energetic particle absorption measurements (see fig. 7 in Buratti et al. 2019). Considering the nature of multiple dust sources in this area, the absolute ejecta mass flux transported outwards from the main rings cannot be directly estimated using the RGO data set alone and is worth further investigation.

5 CONCLUSIONS

We have analysed the composition of ice grains during the penultimate phase of the Cassini mission, the so-called RGO in 2016 and 2017, with perikrones close to the Janus/Epimetheus ring. The compositions of three major types of ice grains detected during the RGO – pure water ice (Type 1), organic-enriched (Type 2) and salt-rich (Type 3) – are similar to those of E ring particles. The detection of these ice grains during the RGO suggests an inward extension of the E ring to at least 2.45 R_S. These ice grains are detected inside the Janus/Epimetheus orbits, overlapping with the tenuous dusty ring of these co-orbital moons. In this context, we suggest that deposition of E ring particles onto the surfaces of Janus and Epimetheus dominates the surface composition of the co-orbital moons.

In the RGO data set, we find Type 1 particles at higher relative abundances than in the central E ring, where Type 2 and 3 particles have much higher fractional abundances than in the RGO region. This is in good agreement with the fact that, due to the much higher relative speeds during the RGO, CDA became more sensitive to smaller grains allowing the observation of a smaller grain size regime (radii mostly 0.1–0.5 μm) than in previous E

ring observations. Type 1 grains are known to be the smallest population and naturally the fraction increases at smaller sizes. Similarly, Type 3 and 2 grains are expected to become depleted at smaller sizes. Additionally, space weathering volatilizes organics in Type 2 grains over time, reducing their sizes while effectively turning them into grains which produce Type 1 spectra (Nölle et al. 2024). The relatively smaller size of Type 1 particles also makes their inward transportation more efficient in comparison to larger particles, increasing their abundance. Similarly, the increased frequency of Type 5 grains, believed to be space-weathered Type 3 particles (Nölle et al. 2024), compared to the central E ring, indicates an older average age of the E ring gains detected at $\sim$2.45 R_S – probably in the order of decades. The reason for the observed pronounced accumulation of Type 5 grains in the central ring plane remains unclear.

Our analysis also suggests that in the region that was sampled during the RGO, a population of impact ejecta from the co-orbital moons Janus and Epimetheus – lying at the large end of the sub-µm size range sampled by CDA – overlaps with the dominant population of smaller particles stemming from the E ring.

Our dynamical and compositional analysis revealed 27 mineral particles on prograde, Saturn bound orbits. This contrasts with the dynamics of mineral dust that CDA observed during the E ring passages, which either comes from outside Saturn or is orbiting Saturn in retrograde motion (Trieloff et al. 2023).

We have found for the first time, a new type of dust with mixed composition in the Saturnian system, which in addition to silicates also carries large quantities of water and seems to be unique to the region between the F ring and the co-orbital moons. The composition of this population, indicative of relatively young particle ages, and the prograde dynamics of the grains, suggests a local source, maybe Janus and Epimetheus, which are known to feed the faint dusty ring along their orbits (Williams & Murray 2011; Seiß et al. 2017; Buratti et al. 2019) with ejecta resulting from IDP impact gardening. The high Cr-silicates can be seen as relatively unique to the sampled region as well. The nearby rings (F and G ring) and moons (Janus, Epimetheus, and Pandora) are potential endogenous sources in the Saturnian system. We also argue that a contribution of silicate grains from the main rings into the region sampled during the RGO, as Fe-poor silicates, similar to those sampled here and known to originate from the main rings, were detected by CDA in the subsequent Grand Finale orbits (Hsu et al. 2018; Linti et al. 2024). This possibility of outward transportation is also supported by our dynamical modelling of main ring ejecta.

ACKNOWLEDGEMENTS

The research in context of this work was supported by the European Space Agency (ESA) under the contract 4000118000/16/ES/JD, and the European Research Council (ERC) Consolidator Grant 724908-Habitat OASIS. Jon K. Hillier thanks the Deutsche Forschungsgemeinschaft (DFG) for funding under grant HI-2157/1-1. The authors thank Prof. Dr. Jürgen Schmidt for valuable discussions, and the reviewer for their very constructive comments.

DATA AVAILABILITY

The periods of CDA data used for this work are listed in Extended Data Table S3 and are archived on the Small Bodies Node of the Planetary Data System (PDS-SBN), at https://sbn.psi.edu/pds/resource/cocda.html.

REFERENCES

Albers N., Sremčević M., Colwell J. E., Esposito L. W., 2012, Icarus, 217, 367
Altobelli N. et al., 2016, Science, 352, 312
Auer A., Sitte K., 1968, Earth and Planet. Sci. Lett., 4, 178
Auer S., Grün E., Srama R., Kempf S., Auer R., 2002, Planet. Space Sci., 50, 773
Brown R. H. et al., 2004, Space Sci. Rev., 115, 111
Buratti B. J. et al., 2019, Science, 364, eaat2349
Buratti B. J., Mosher J. A., Johnson T. V., 1990, Icarus, 87, 339
Clark R. N. et al., 2008, Icarus, 193, 372
Clark R. N. et al., 2012, Icarus, 218, 831
Cuzzi J., Clark R. N., Filacchione G., French R. G., Johnson R., Marouf E., Spilker L., 2009, in Dougherty M. K., Esposito L. W., Krimigis S. M., eds, Saturn from Cassini-Huygens. Springer, Dordrecht, p. 459
Dikarev V. V., Krivov A. V., 1998, Sol. Syst. Res., 32, 128
Fiege K., Trieloff M., Hillier J. K., Guglielmino M., Postberg F., Srama R., Kempf S., Blum J., 2014, Icarus, 241, 336
Filacchione G. et al., 2013, ApJ, 766, 76
Fischer C., Postberg F., Altobelli N., Nölle L., Albin T., 2018, EPSC, 12, 1279
Gehrels T. et al., 1980, Science, 207, 434
Grün E. et al., 1992a, Space Sci. Rev., 60, 317
Grün E. et al., 1992b, A&AS, 92, 411
Grün E., Krüger H., Srama R., 2019, Space Sci. Rev., 215, 1
Hamilton D. P., Burns J. A., 1994, Science, 264, 550
Hedman M. M., Burns J. A., Hamilton D. P., Showalter M. R., 2012, Icarus, 217, 322
Hedman M. M., Helfenstein P., Chancia R. O., Thomas P., Roussos E., Paranicas C., Verbiscer A. J., 2020, AJ, 159, 129
Hillier J. K. et al., 2007, MNRAS, 377, 1588
Horányi M., Burns J. A., Hedman M. M., Jones G. H., Kempf S., 2009, in Dougherty M. K., Esposito L. W., Krimigis S. M., eds, Saturn from Cassini-Huygens. Springer, Dordrecht, p. 511
Horányi M., Juhász A., Morfill G. E., 2008, Geophys. Res. Lett., 35, L04203
Hsu H.-W. et al., 2018, Science, 362, eaat3185
Hunziker S. et al., 2022, Planet. Space Sci., 220, 105536
Johnson R. E., Famá M., Liu M., Baragiola R. A., Sittler E. C., Jr, Smith H. T., 2008, Planet. Space Sci., 56, 1238
Jurac S., Johnson R. E., Richardson J. D., 2001a, Icarus, 149, 384
Jurac S., Johnson R. E., Richardson J. D., Paranicas C., 2001b, Planet. Space Sci., 49, 319
Kempf S. et al., 2008, Icarus, 193, 420
Kempf S., Beckmann U., Schmidt J., 2010, Icarus, 206, 446
Kempf S., Horányi M., Hsu H.-W., Hill T. W., Juhász A., Smith H. T., 2018, in Schenk P.M., Clark R. N., Howett C. J. A., Verbiscer A. J., Waite J. H., eds, Enceladus and the Icy Moons of Saturn. Univ. Arizona, Tucson, p. 195
Khalisi E., Srama R., Grün E., 2015, Adv. Space Res., 55, 303
Khawaja N. et al., 2019, MNRAS, 489, 5231
Khawaja N., Postberg F., Schmidt J., 2017, LPSC, 48, 2005
Koschny D., Grün E., 2001, Icarus, 154, 402
Krüger H., Krivov A. V., Hamilton D. P., Grün E., 1999, Nature, 399, 558
Linti S. et al., 2024, MNRAS, submitted
Lodders K., 2003, ApJ, 591, 1220
Napoleoni M., Klenner F., Khawaja N., Hillier J. K., Postberg F., 2023a, ACS Earth Space Chem, 7, 735
Napoleoni M. et al., 2023b, ACS Earth Space Chem., 7, 1675
Nölle L. et al., 2024, MNRAS, 527, 8131
Northrop T. G., Hill J. R., 1982, J. Geophys. Res., 87, 6045
Porco C. C., Cassini Imaging Team, 2006, Int. Astron. Union Circular, 8759, 1
Porco C. C., Danielson G., Goldreich P., Holberg J., Lane A., 1984, Icarus, 60, 17
Postberg F. et al., 2018, Nature, 558, 564
Postberg F., Kempf S., Hillier J. K., Srama R., Green S. F., McBride N., Grün E., 2008, Icarus, 193, 438

Postberg F., Kempf S., Rost D., Stephan T., Srama R., Trieloff M., Mocker A., Goerlich M., 2009a, Planet. Space Sci., 57, 1359
Postberg F., Kempf S., Schmidt J., Brilliantov N., Beinsen A., Abel B., Buck U., Srama R., 2009b, Nature, 459, 1098
Postberg F., Schmidt J., Hillier J. K., Kempf S., Srama R., 2011, Nature, 474, 620
Ratcliff P. R., McDonnell J. A. M., Firth J. G., Grün E., 1992, J. British Interplanet. Soc., 45, 375
Seiß M., Srama R., Hoffmann H., Spahn F., 2017, AAS/DPS Meeting, 49, 104.05
Smith B. A. et al., 1981, Science, 212, 163
Srama R. et al., 2004, Space Sci. Rev., 114, 465
Trieloff M., Fischer C., Postberg F., Schmidt J., 2023, EGU General Assembly, EGU23–16469
Verbiscer A. J., French R., Showalter M., Helfenstein P., 2007, Science, 315, 815
Verbiscer A. J., Helfenstein P., Buratti B. J., Royer E., 2018, in Schenk P.M., Clark R. N., Howett C. J. A., Verbiscer A. J., Waite J. H., eds, Enceladus and the Icy Moons of Saturn. Univ. Arizona, Tucson, p. 323
Waite J. H. et al., 2004, Space Sci. Rev., 114, 113
Wiederschein F. et al., 2015, Phys. Chem. Chem. Phys., 17, 6858
Williams G. A., Murray C. D., 2011, Icarus, 212, 275
Winter O. C., Souza A. P. S., Sfair R., Winter S. M. G., Mourão D. C., Foryta D. W., 2018, ApJ, 852, 8
Ye S. Y. et al., 2018, J. Geophys. Res. Space Phys., 123, 4952

SUPPORTING INFORMATION

Supplementary data are available at *MNRAS* online.

Fring_Supplement_final.pdf

Please note: Oxford University Press is not responsible for the content or functionality of any supporting materials supplied by the authors. Any queries (other than missing material) should be directed to the corresponding author for the article.

This paper has been typeset from a TEX/LATEX file prepared by the author.